Ore mineralogy and uraninite trace element chemistry of hydrothermal polymetallic U-Ag-(Co-Ni-As-Bi-Sb-Cu) vein deposits, Eldorado Mine, Port Radium, NWT

By

Matthew Bailey

A Thesis Submitted to Saint Mary's University, Halifax, Nova Scotia in Partial Fulfillment of the of the Requirements for the Degree of Geology.

May 1st, 2017, Halifax Nova Scotia

Approved: Dr. Jacob Hanley

Associate Professor

Department of Geology

Date: May 1st, 2017

Ore mineralogy and uraninite trace element chemistry of hydrothermal polymetallic U-Ag-(Co-Ni-As-Bi-Sb-Cu) vein deposits, Eldorado Mine, Port Radium, NWT

Matthew Bailey

ABSTRACT

The paragenetic sequence of uranium enriched polymetallic deposits at the Eldorado mine in the N.W.T, Canada, is poorly understood. Few studies have used modern analytical techniques to characterize the deposit. This study aims to update paragenetic models by use of petrographic work as well as SEM analysis. This data will be used in conjunction with LA-ICPMS to characterize the trace element composition of uraninite (interpreted to be UO_2, U_3O_8 mixture). The data show that there are alternating sequences of coprecipitation between uraninite and Co-Ni arsenides. This indicates that the fluid is carrying multiple metals (U, Ni and Co) simultaneous and that a major factor in their precipitation is an increase in fO_2. Our paragenetic sequence closely follows previous models

Date: May 1 2017

Table of Contents:

Figure List:

Table List:

1.0 Introduction

The Eldorado mine, located at Port Radium, NWT, is one of several mines comprising the Echo Bay-Eldorado-Camsell River ('EEC') mining district within the Great Bear Lake magmatic zone. Mineralization at the Eldorado comprises a polymetallic vein system of the "five metals" association (e.g., Cobalt and Thunder Bay districts, Ontario) with a substantial enrichment in uranium. While uncommon for this style of deposit globally, such uranium enrichment is not unique to the Eldorado mine (e.g., Jachymov deposit, Czech Republic; Alexandre et al. 2015). Other deposits in the EEC (e.g., Echo Bay, Terra/Silver Bear and Norex Deposits) are not uranium rich and were mined only for their substantial former reserves of silver (Kissin, 1992).

G.A LaBine first discovered the Eldorado deposit in 1930 with production of the mine occurring between 1933 and 1960 by the Eldorado Mining Company. The mine produced radium with uranium as a by-product for the pharmaceutical industry, followed by a focus in uranium production during the 1940s, and eventually produced silver as an additional commodity (Jory, 1964). The Eldorado mine Canada's only uranium producer from 1938 to 1955 and produced approximately 6000 tonnes of uranium over 22 years from (Ruzicka and Thorpe, 1996). Compared to the surrounding mines in the area, Eldorado produced larger quantities of its commodities (Table 1) (Silke, 2009). Eldorado also produced Ni, Co and Pb and these metals were sold off as a by product

This deposit has seen very little in terms of modern interpretation or analysis by modern methods since Kidd and Haycock (1932). A more recent paper constrains the age of deposition between the 1.72 Ga Cleaver Dikes and the 1.59 Ga Western Channel Sheets (Gandhi et al., 2013). This study aims to determine the paragenesis of the Eldorado ores to characterize the mineralization events and to determine if the mineralization events were produced by similar or different fluids. To achieve this, we will be using petrographic observations and scanning electron microscope to identify minerals and examine microscopic texture, and a laser ablation inductively coupled plasma mass spectrometer (LA-ICPMS) to determine trace element abundances in uraninite, with a goal of determining textural chemical variations to identify specific phases.

Table 1: Production of mines in the Eldorado, Echo Bay and Camsell River area. Production of mines in the Great Bear Lake magmatic zone and surrounding areas (Silke 2009). Time frame is the first and last year of production, time gaps may exist.

Mine	Operating from	Commodities	Production
Eldorado	1933-1982	U_3O_8,Ra,Ag	13 402 000lbs U_3O_8, 450g Ra, 13 371 382 oz Ag, 2389 tons Cu
Echo Bay	1964-1974	Ag,Cu	23 564 461 oz Ag, 4 505 tons Cu
Contact Lake	1935-1980	Ag,U_3O_8	678 000 oz Ag, 6 933 lbs U_3O_8
Norex	1970-1983	Ag	2 066 744 oz Ag
Northrim	1971-1978	Ag	30 000 oz Ag
Smallwood Lake	1979-1983	Ag	169 720 oz Ag
Terra (Silver Bear)	1969-1985	Ag,Cu	14 236 325 oz Ag, 2 284 tons Cu

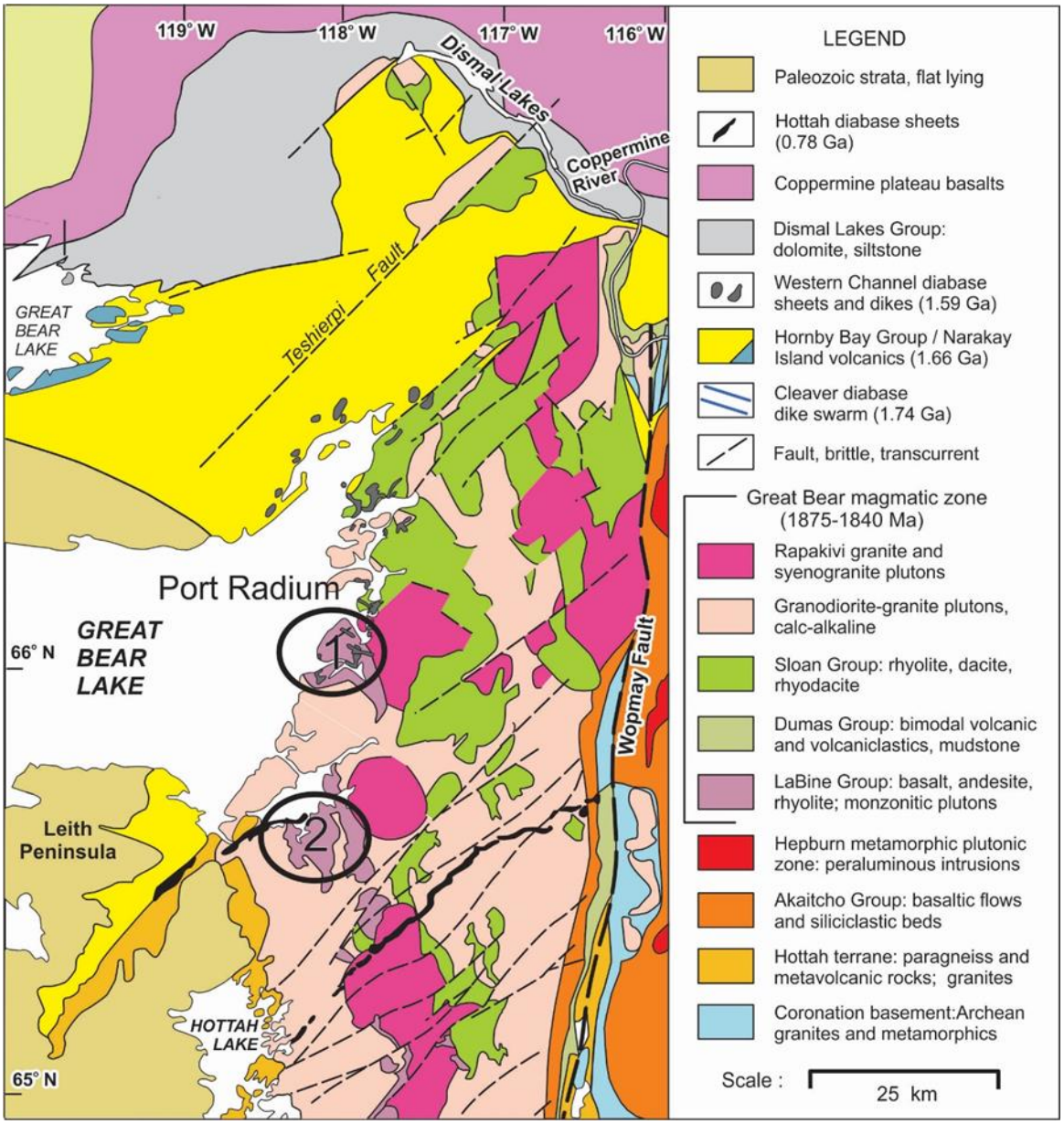

Figure 1: Area Map. Lithostratigraphic map of the Great Bear Lake magmatic zone of the N.W.T. ***1*** denotes both the Eldorado mine (site of study) and the Echo Bay mine, while the ***2*** indicates the Camsell River area containing the Norex, Northrim, Smallwood Lake and Terra/Silver bear mines. This map has been modified from Gandhi et al. (2013).

A trace element database of uraninite from multiple worldwide deposits will be created to compare of differences in uraninite composition from different deposits. By use of petrography and LA-ICPMS we will determine the paragenesis and compare our sequence with the “5 stages” of deposition.

1.1 Geological setting

The Great Bear Lake magmatic zone (GBLMZ) is an ~100km wide area comprising mainly volcanics and volcanoclastics of predominantly intermediate compositions. This zone represents an ancient calk-alkaline continental arc setting on the western edge of the Wopmay Orogen. (Gandhi et al., 2013). It includes both mafic/felsic flows, tholeiitic basalts and ash flows. These units were subsequently intruded by numerous plutons and sills (Reardon, 1992) with U-Pb age of zircons between 1875 Ma to 1850 Ma. (Changkakoti et al., 1986)

The area of interest is located within a 10km thick section known as the McTavish Supergroup. This supergroup comprises the LaBine, the Sloan and the Dumas group. The LaBine Group, comprises the Port Radium, Echo Bay and the Cameron Bay formation which are successions of intermediate lava flows, pyroclastics and sedimentary rocks. (Reardon, 1992). The LaBine group was later intruded by plutons of quartz monzonite and by syenogranites (~1858 to 1843 Ma (Gandhi et al., 2013)).

The oldest formation present in the GBLMZ is Port Radium, which contains predominantly sedimentary rocks, from fine-grain coarsening upwards to subaerial conglomerates with pyroclastics (Reardon, 1992).

The Echo Bay Formation comprises of andesitic flows, epiclastic rocks and breccias, which lie over the Port Radium formation. This formation begins as a mixture of clastic rocks and flows and evolves into being dominated solely by flows (Reardon, 1992). The epiclastic rocks present consists of volcanic sediments, conglomerates, tuffs and debris flows. The andesitic flows contain plagioclase phenocrysts with several of the flows showing amygdules and flow top breccias. (Reardon, 1992).

Figure 2: Fault bounded vein mineralization map. Distribution map of the Eldorado/Echo Bay mine in Port Radium, N.W.T. Modified from Gandhi et al. (2013).

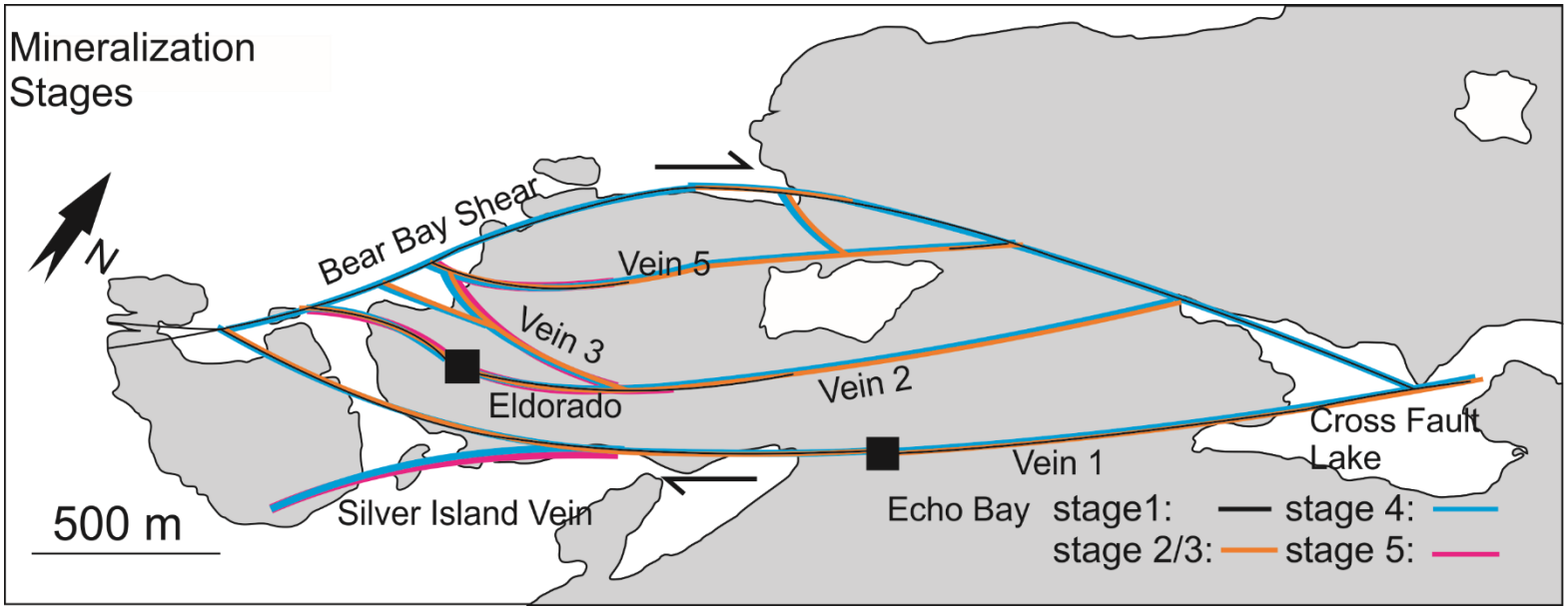

These formations were intruded several times after deposition. Two of these are of great interest to the area as they constrain the timing of deposition. The first is the Cleaver dyke swarm, at an age of approximately 1.74 Ga. This is a northwest trending, steeply dipping system of diabase dykes throughout the Echo Bay area. This set of dykes predates the ore mineralization, as it occurs as fragments in mineralized breccias (Gandhi et al., 2013). The second is the 1.59 Ga Western Channel diabase present in the town of Port Radium. This is an east dipping swarm which intrudes the Cleaver dykes and the formations overlying the LaBine Group (Gandhi et al., 2013).

The samples were sourced from the Eldorado mine, located in Port Radium which has outcrops from both the Port Radium and Echo Bay Formations (Fig 1). The mine contains fault hosted quartz veins trending in a NE direction. These faults are believed to be related to the McDonald fault system, which resulted from the accretion of the Nahanni-Fort Simpson terranes (or an event farther west) on the western side of Hottah Terrane (Gandhi et al., 2013). These faults were reactivated after the emplacement of the Cleaver dykes allowing for the 5 stages of mineralization (Gandhi et al., 2013). Fig. 2 shows the distribution of the mineralization stages in the faults in the area of interest. Ore host veins within the fault system have varying characteristics. Vein thickness varies from an inch thick to 30ft thick and some veins occur in ore breccias. Gangue minerals include predominantly quartz, carbonates chlorites and white micas as the most dominant.

2.0 Methods:

The rock samples were collected by Professor J. Hanley and MSc candidate Corwin Trottier from a storage facility at the Geological Society of Canada, Ottawa. The samples were originally collected in the field by D.F. Kidd and M.H. Haycock. The samples were chosen to represent varying stages of mineralization and different veins present at the Port Radium mine.

All samples were cut at Saint Mary's University. Due to the nature of the samples, some being radioactive, the cut radioactive samples were sent to SRC (Saskatchewan Research Council) and the non-radioactive samples were sent to Vancouver Petrographics to be made into both thin and thick sections.

The samples were investigated using several analytical methods. These methods included petrographic study, Scanning Electron Microscope (SEM), Laser Ablation Inductively Coupled Plasma Mass Spectrometry (LA-ICPMS) and Raman Spectroscopy.

2.1 Petrography

A petrographic microscope was used to identify minerals in both transmitted and reflected light and to classify and understand the paragenetic relationships/textures shown by ore and gangue minerals between the samples.

2.2 SEM

A TESCAN MIRA 3 LMU Variable Pressure Schottky Field Emission Scanning Electron Microscope (SEM) at the Regional Analytical Centre at Saint Mary's University was used to quantify major elements in ore and accessory minerals, and image mineral textures l associations. Back-scattered electron (BSE) image of the grains in a carbon-coated polished thin section were produced to examine mineral textures. The SEM has a maximum resolution of 1.2 at 30kv. Energy dispersive spectrometry (EDS) was used to determine mineral composition and to identify minerals. It is equipped with an INCA X-max 80 mm2 silicon-drift detector (SDD) EDS system. The data was interpreted by INCA software, giving data in weight percent. Once data was collected, the values were recalculated after the removal of Carbon and Oxygen values. Carbon due to true values being inseparable from the carbon coating and oxygen was removed due to the minerals of interested being arsenides and sulphides.

2.3 LA-ICPMS

Comprehensive trace element (LILE, HFSE, transition metals and semi metals, and REE) analyses (spot and rastered maps) of uraninite were obtained by laser ablation inductively-coupled plasma mass spectrometry (LA-ICPMS) at the Department of Earth Sciences, University of New Brunswick. The measurements were acquired using a pulsed (20 ns) 193 nm ArF Excimer laser ablation system (Resonetics RESOlution M-50) coupled to an Ar- plasma quadrupole ICP-MS (Thermo Scientific X Series II). The ablation system employs a two-volume Laurin Technic sample cell. Measurements were done with a 10 ms dwell time for each analyte isotope, a forward torch power of 1450 W, gas flow rates of 0.8

l/min, 0.65 l/min and 6 ml/min for Ar, He and N2, respectively, and laser fluence of 6 J/cm2. The raw data (in cps vs. time) were quantified using the Iolite software package (Paton et al. 2011), with synthetic NIST SRM 610 glass used as an external reference material to calibrate analyte sensitivities and mean value U (70 wt. % determined by SEM-EDS) as the internal standard for uraninite. This value is slightly off of the true values for uraninite which are show to be 65 wt % ± 5% wt. The BHVO-2G reference glass was used as a QC monitor. Three thick sections were analyzed to acquire trace element data (both REE's and metals) from uranium phases in the samples. Thick sections were used due to the concern that thin sections might be too thin for laser ablation to be an effective means of analysis.

Selected uraninite grains were also mapped using LA-ICPMS. To prepare for laser ablation, the samples were cleaned, to ensure no carbon coating remained from when they were subjected to SEM BSE. A short, wide radius beam was applied to the mapping area prior to mapping to remove any arsenic coating/contamination from the area as it can produce erroneous results from prolonged washout times.

2.4 Raman Spectroscopy

Preliminary Raman analyses were performed on an unknown uranium phase in order to identify it. It was conducted at Saint Mary's University using a Jobin-Yvon Horiba LabRam HR confocal Raman microscope with an 800 mm spectrograph and Synapse 1024 x 256 pixel CCD detector. A 600 groves/mm grating and 15 µm confocal hole size were used during spectrum collection, with a 532 nm (green) Nd-YAG laser (105 mW laser power at objective) at 1% power, was used for excitation, directed through a 50x objective. Pure silicon was used as a frequency calibration standard. Spectrum collection over the range 100-4500 cm-1 was done at an acquisition of 20s per accumulation with 3 accumulations obtained per analysis.

3.0 Results

3.1 Models

Both uranium enriched and uranium absent five metal deposits (also known as polymetallic) have been characterized, leading to the development of multiple models

throughout the years (Gandhi et al., 2013; Kissin, 1992). We will be exclusively looking at the models for the uranium-enriched five metal deposits. The models we will be using as a basis, is that of Kissin (1992) and Gandhi et al. (2013). Table 2 summarizes the two different paragenetic interpretations. The descriptions are the major minerals of each stage. Other minor minerals may be present, such as quartz or carbonates.

3.2 Ore mineralogy and textures

A total of 18 polished sections (15 thin sections and 3 thick sections) of ore veins and wall rock were examined using the petrographic microscope and SEM, and mineral phases were identified. Native metals, sulphides, aresnides, sulpharsenides, carbonates, quartz and several oxides were identified. They were based on the weight percent values given by the INCA software and a comparison with mineral values from the Web Mineral Mineral database.

Several wall rock phases are present; it is difficult to determine their mineralogy due to alteration. Massive hematization and chloritization replaces the minerals and this occurred before the precipitation of many of these following stages. We do know that these are the volcanics from previous studies.

Multiple episodes have formed uraninite and coffinite, evident by textural and chemical difference between them. Within this text, uranium phases will be referred to as primary and secondary occurrences. Primary uranium phases are characterized by open growth texture, which in this study is mainly botryoidal uraninite. Secondary uranium phases which seem to be remobilisations characterized by disseminated uranium phases. Fig. 3a to 3e show 3 occurrences of primary uraninite, with no spatial relationship between them. Fig. 3b is the inset in Fig. 3a, giving a magnified view of the fractures and rim of the botryoidal uraninite. Within the fractures and along the edge of the grains, there is cobaltite, a cobalt sulpharsenide. Within the rim of the uraninite grain are inclusions that are not associated with fractures. The nature of the inclusions will be discussed in a later section. Within the carbonates and infilling voids in the sulpharsenides, chalcopyrite and sphalerite.

Table 2: Model Summary. Summary of two paragenetic sequences of U enriched, five metals deposits. Kissin (1992) describes a genetic model to be potentially applied to deposits worldwide, where as Gandhi et al. (2013) describes a model applied to Port Radium.

	Kissin Model (1992)			Gandhi et al. Model (2013)	
Stage #	Name	Description	Stage #	Name	Description
1	Barren	Quartz, potentially minor amounts of sulphides	1	Quartz	Barren quartz + potentially hematite and pitchblende
2	Uraninite	Uraninite and quartz	2	Pitchblende	Pitchblende + carbonates
3	Ni/Co arssenide	Native silver in association with	3	Arsenide	Ni/Co/Fe sulph/arsenides + native Ag/Bi
4	sulphide	Cu/Pb/Zn/Sb/Ag sulphides + Ag minerals in a carbonate/quartz	4	Sulphide	Cu/Zn/Pb/Sb/Ag/Mo sulphides
5	Late stage	Calcite + barite/fluorite	5	Carbonate	Carbonates + Native Ag/Bi
			6	Native Silver	Native Ag/Bi

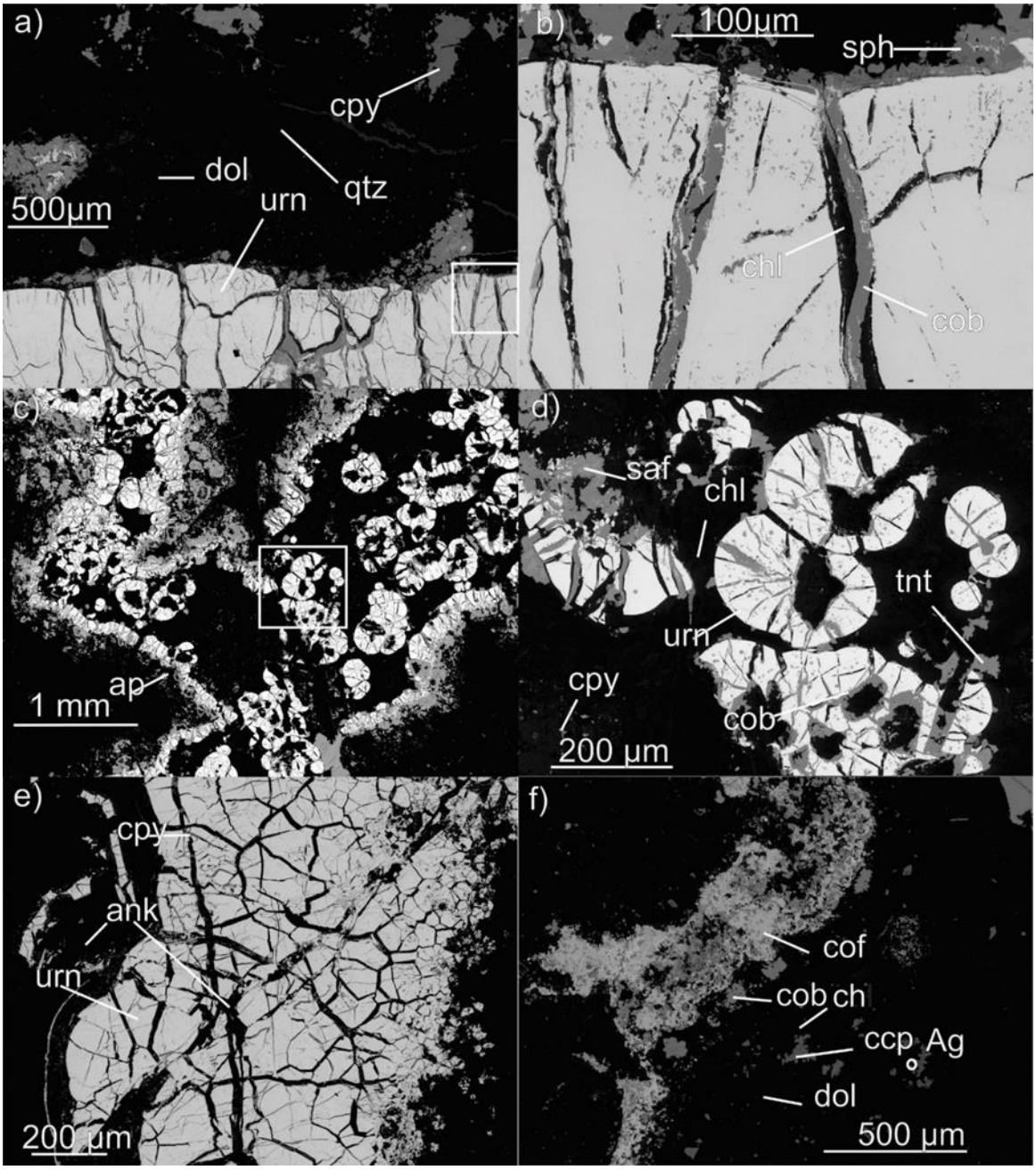

Figure 3: Uraninite occurrences and textures. a) fractured botryoidal uraninite infilled by cobaltite, followed by sulphide bearing carbonates. Square denotes inset for figure 3b). b) fracture botryoidal uraninite. c) Botryoidal uraninite occurring in wallrock fracture with inset d). d) fracture and infil by sulpharsenides and arsenides. Some sulphides such as tennantite (tnt) and chalcopyrite (cpy). e) Botryoidal uraninite suspended in a carbonate gangue. Heavily fractured and later infilled by sulphide. f) later disseminated coffinite stage with sulphides and sulpharsenides. (ap=apatite, ch=chlinochlore, Ag=native silver, ank=ankertier, sph=sphalerite)

Fig. 3c and 3d are another primary occurrence, this time hosted within a fractured wall rock. This uraninite is also botryoidal in nature, the main difference visually between these images and the previous is the axis along which they are cut. With these samples, however we can see a similar history, of fracturing and infilling by cobaltite and safflorite, followed by sulphide bearing carbonates. This uraninite also has inclusions. Fig. 3e shows a more heavily fractured occurrence of primary uraninite, the curvature indicative of botryoidal texture is visible on the left-hand side of the image, with the right hand being where the mineral was likely previously attached to the wall rock. The uraninite is surrounded by ankerite. The sulphides found present in all occurrences are similar with chalcopyrite being dominant. Fig. 3f shows one occurrence of a secondary coffinite, disseminated with cobaltite within the dolomitic matrix.

Fig. 3a shows multi-episodic precipitation of primary uranium phases, and subsequent alteration. In Fig. 4b we see early cobaltite in contact with the wall rock followed by alternations of uraninite and cobaltite followed by coffinite. Coffinite replaces and fractures the uraninite, cobaltite and wall rock, indicating that this is not a primary phase (Figs. 4b, c, e, f).

The native metals found in the samples are strictly silver and bismuth. Native silver occurs first in the form of dendrites. This native silver occurs coevally with Ni-Co arsenides forming zoned dendrites that alternate between silver and Ni,CoAs. Inclusions of arsenides found in the silver dendrites support this. This fluid shows an initial composition rich in arsenic as it comprises of both safflorite and skutterudite, both of which are di-arsenide phases (Figs 5a and b). This multi-stage precipitation of silver dendrites shifts to a precipitation of solely Ni-Co arsenides towards the end of this stage.

Silver and arsenide precipitation is followed by a dolomite phase which fractures into dendrites and partially to completely replaces silver (Fig. 5c, b). A later phase of native silver is found in association with later carbonates and sulphides.

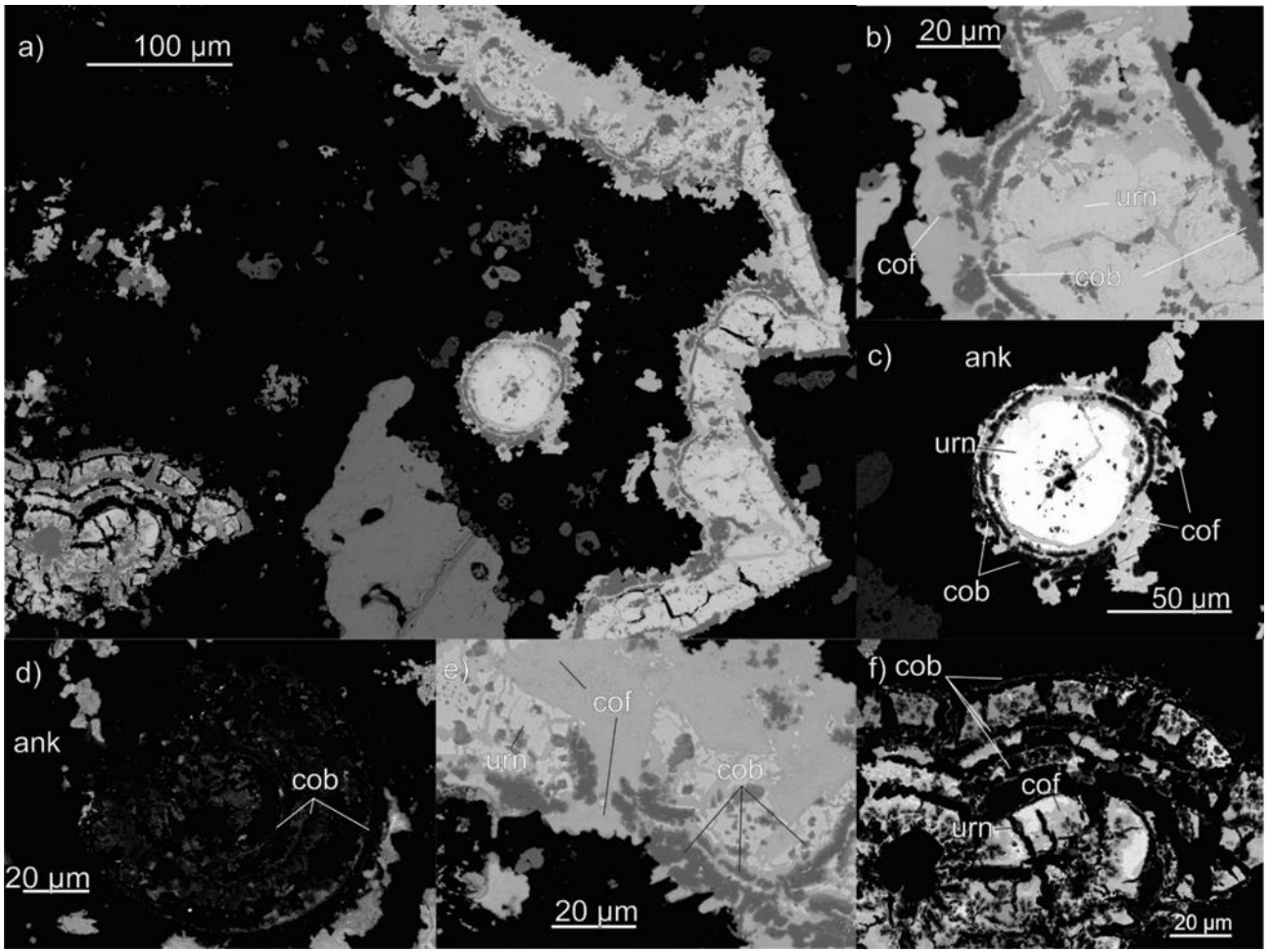

Figure 4: Coffinite alteration of repetitive uraninite. Coffinite/Uraninite (cof/urn) along wall rock displayed in a). b) and e) show coffinite replacing uraninite, displacing the cobaltite (cob) present. c) Botryoidal section showing the interactions of all phases + ankerite (ank) matrix. d) and f) demonstrate the alternating sequences of sulpharsenides and uranium bearing phases with d) showing a complete dissolution with only the cobaltite shell remaining.

The composition of the arsenides is highly variable, however a trend is visible in the larger grains. As we move rim-ward from the core dendrites, we see a gradational change in the colour (Fig. 5d). We notice a bright phase change into a briefly darker phase before a sharp contact between it and another bright phase. This darker portion represents a brief enrichment of sulphur, resulting in a shift of mineralogy from the nickeline and langisite to cobaltite and gersdorfite [endmembers having a composition of (Co,Ni)AsS]. This period is quite brief as it returns to a sulphur lacking, arsenic rich composition such as rammelsbergite or skutterudite [(Ni,Co)As3 and NiAs2 respectively].

Bismuth came at a later interval of the arsenide stage. Bismuth fractures the dendrites and it removed the silver core of the dendrites and it heavily fractured the Ni-Co arsenides phases surrounding it. This event is shown as well in Fig. 5d. The bismuth composition has changed in the thin fractures increase in sulphur content increases to where it becomes bismuthenite, this may be it removing the sulphur from the environment, but this is interpretation is solely based on textural and chemical relationships.

Multiple quartz phases are present in the paragenetic sequence and these characterized by texture. Several of the samples show large equant grains of quartz followed by sulphide bearing carbonates infilling gaps between the crystals. Within the large equant grains, we find open space filling, acicular hematite. Quartz can also occur as small equant grains that surround the arsenides previously mentioned. They can also be seen as reprecipitated quartz.

None-alteration based hematite is almost exclusively in acicular form, however it does not interact with the calcite present so its relationship to timing is hard to infer. Coarse grained quartz are follows by a grainy calcite phase that begins to fracture once again the Ni-Co phase, this carbonate is low in calcium but high manganese. This phase remobilises the bismuth and replaces it in the dendrite voids. This relationship has been seen before in Fig. 5c (the small thin veins of magnesite cutting through the dendrites) and as well in Fig. 5e. This episode has been seen to cut across the quartz phases. The relationship between the smaller quartz phases, carbonates and drusy arsenides can be seen in Fig. 5f.

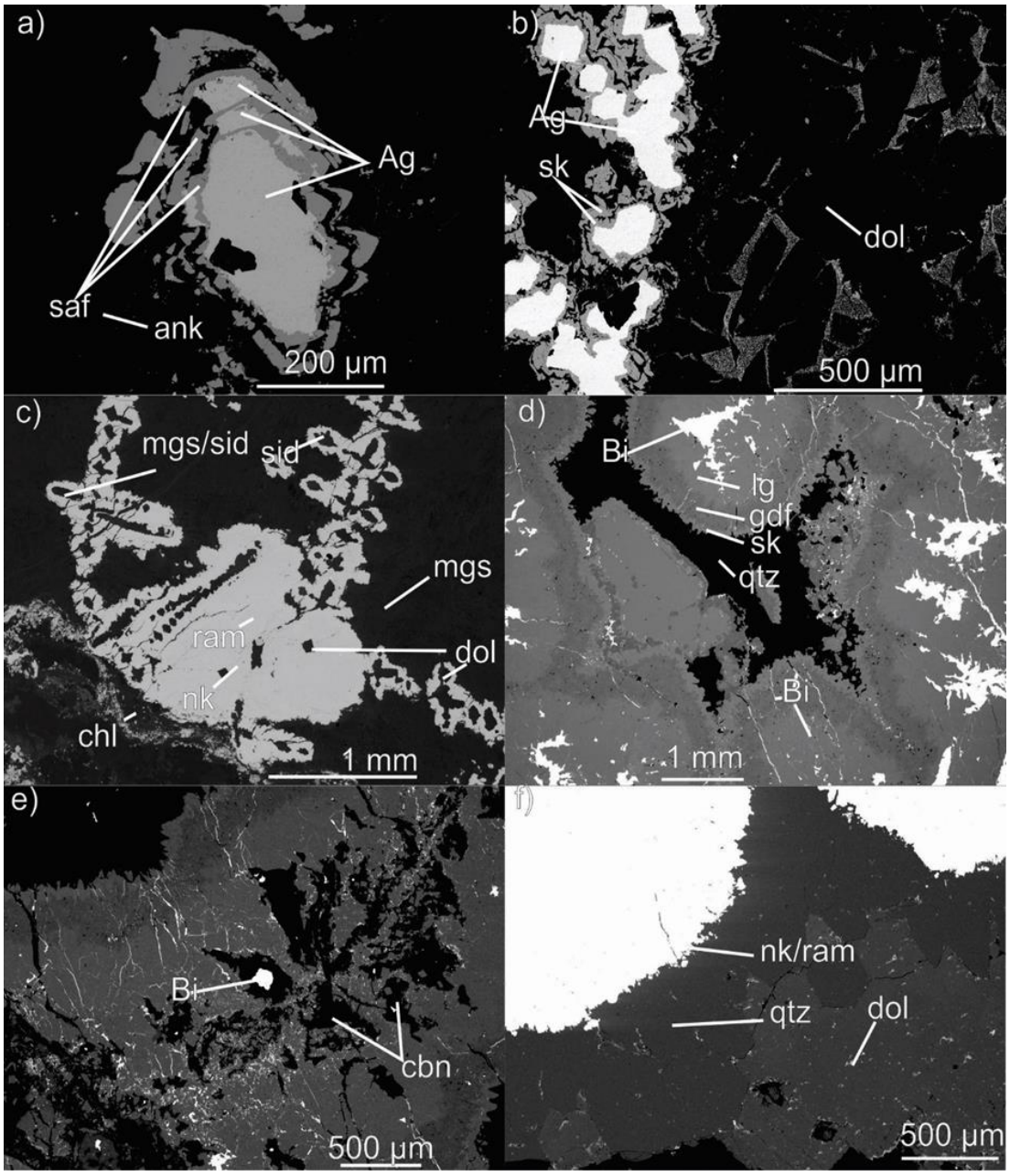

Figure 5: **Dendrite evolution** the developement and evolution of the native silver (Ag) dendrites. a) alternating silver and safflorite (saf) episodes create the core of dendrites. b) these dendrites become replaced by carbonates(dol, cbn), sometimes leaving the arsenide shell intact as in c). d) evolution of arsenide dendritic shell that shows a brief sulphur enrichment, becomes infilled with native bismuth (Bi), shown by radiating fractures from core of dendrites. e) displays a later carbonate episode which fractures the core again, replacing and removing bismuth. f) shows euhedral growth of quartz crystals along the edge of drusy texture arsenides (nickeline/rammelsbergite are nk/ram respectively).(mgs= magnesite, sid=siderites, langisite=lg, gersdorfite=gdf, sk=skutterudite)

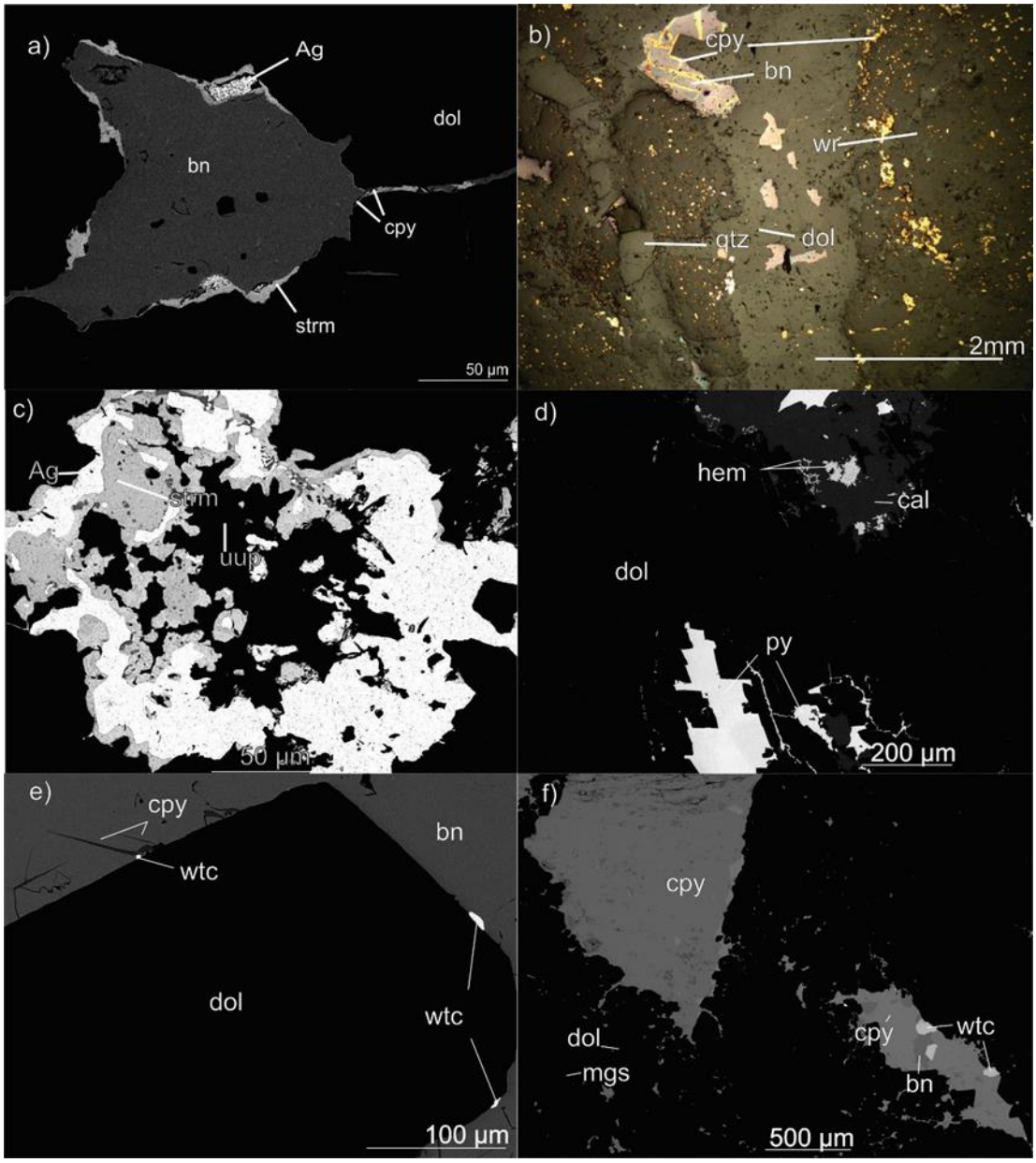

Figure 6: Sulphide and silver associated textures. a) bornite(bn) showing boxwork replacement by chalcopyrite (cpy). Accumulation of native silver (Ag) and stromeyerite (strm) along the boundary between the sulphide and the dolomite (dol) matrix. b) relected light image of interacting cpy, bn and various gangue minerals within a fractured wallrock. Sulphides found disseminated throughout the wall rock. c) Ag and stromeyerite (strom) encasing an unknown uranium phase (uup), indication of a very late uranium phase. d) pyrite infilling voids within a carbonate matrix. Accular hematite (hem) hosted within calcite (cal). e) and f) show more replacement and open space filling texture between various sulphides and carbonate phases. (mgs=magnesite, wtc= wittichenite)

Table 3: **Mineral composition.**

Sample #	Site	Spectrum Ag	Ag	Al	As	Bi	Ca	Co	Cu	Fe	Mg	Mn	Ni	Pb	S	Sb	Si	U	Zn	Total	Mineral
714-2	12	1			47.65			43.24		2.79					4.59		1.73			100	safflorite
714-2	12	4			40.49			38.64		2.69					17.83		0.35			100	cobaltite
714-2	6	142			73.21			26.79												100	skutterudite
714-2	5	1			64.91			2.09					31.71		1.29					100	rammelsbergite
793-3	9	3			54.49			20.18					18.17		7.16					100	langisite
289-1	4	3							0.63	0.46					36.91		0.45		61.55	100	sphalerite
850-1	1	3			56.78								40.63			2.59				100	nickeline
850-1	1	12					55.93			8.8	30.4	4.87								100	dolomite
704-2	6	4		1.19			2.71		1.67								13.8	80.63		100	coffinite
609-1	3	15							55.28	11.2					33.52					100	bornite
608-2	9	1			52.42			6.3		1.44			20.94		18.38		0.51			100	gersdorfite
714-2	11	2				85.66									14.34					100	bismuthinite
843	2	3				44.31			38.64	0.99					16.07					100	wittichenite
704-1 Thick	2	1					47.99			4.54	3.55	43.92								100	kutnorhorite
704-1 Thick	2	2					83.17			1.63		15.21								100	calcite
704-1 Thick	2	3					51.87			6.47	22.36	19.31								100	ankerite
704-1 Thick	2	5							32.4	28.91					38.69					100	chalcopyrite
704-1 Thick	2	6			17.61				38.49	2.56					29.89	5.33			6.12	100	tennantite
704-1 Thick	3	6		10.33			2.64			36.59	11.29	4.4					34.02			99.27	clinochlore
704-1 Thick	6	1			12.67			1.19	36.5	1.21					28.95	12.81			6.66	99.99	tetrahedrite
704-1 Thick	7	4	2.66		12.11				39.58	1.32					27.7	9.84			6.77	100	Ag-rich tennantite
608-2	1	11					0.87			27.6	69.21	2.33								100	magnesite
608-2	6	2				20.71			25.85	6.04				24.95	22.45					100	miharaite
704-1	11	2	86.99							5.1					11.23					98.73	argentite
704-2	8	2	0.75				2.48					0.66		4.68			0.51	90.92		100	uraninite
843	4	1	56.33						31.03						12.64					100	stromeyerite

The carbonate phases in this system are extremely varied in both textures and compositions, the later which will be discussed in the following section. The carbonates are displaying massive texture as well as clear equant grains of calcite of varying sizes.

Only one carbonate phase is described to be associated with sulphides, this being the 4th stage in the models (Table 2). The sulphides range from chalcopyrite/bornite, galena, tetrahedrite-tennantite as well as a more unique sulphide, wittichenite. The chalcopyrite has been observed as both isolated grains and showing box-work texture with the bornite. Multiple sulphide phases are seen to occur together within a single vein as in Figure 6b.

These sulphides occur with a later silver phase, comprising of both native silver as well as the appearance of stromeyerite (AgCuS) (Figure 6a). It is in this sulphide-silver stromeyerite assemblage that we also see the unknown uranium phase (abbreviated to uup) indicating another unique phase of remobilization. Figure 6c) shows the relationship of the silver and stromeyerite encompassing the uup in the dolomite/sulphide matrix of stage 4. The uup composition will be discussed in section 3.4. Pyrite (Fig. 6d) can be seen infilling voids and fractures of the dolomite. In close proximity to the dolomite, acicular hematite is encased in a calcite matrix. Sparse wittichenite, chalcopyrite and bornite are all see in encompassing (Fig. 6e) or infilling (Fig. 6f) dolomite crystals or matrix. Table 3 shows a summary of the major minerals found within the system.

3.3 Accessory Mineral Chemistry

A large variation in chemical composition of Ni-Co minerals and carbonates was observed. The Ni-Co phases show variations between end-members (some inclusion of Fe is present as well) as well as the inclusion of sulphur into the structure during the brief enrichment period.

The Ni-Co aresnides have been plotted on two diagrams in Fig. 7. Figure 7a shows a triplot diagram illustrating the relationship between nickel, cobalt and arsenic. It shows that many samples plot between nickeline or rammelsbergite for nickel-rich samples or plotting near Co-rich safflorite. A dozen samples plot in the middle of the diagram, representing Ni- rich

a)

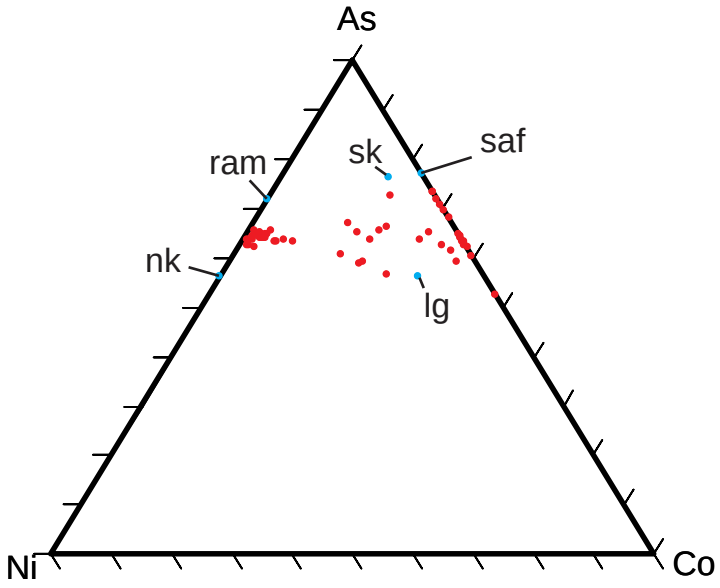

b)

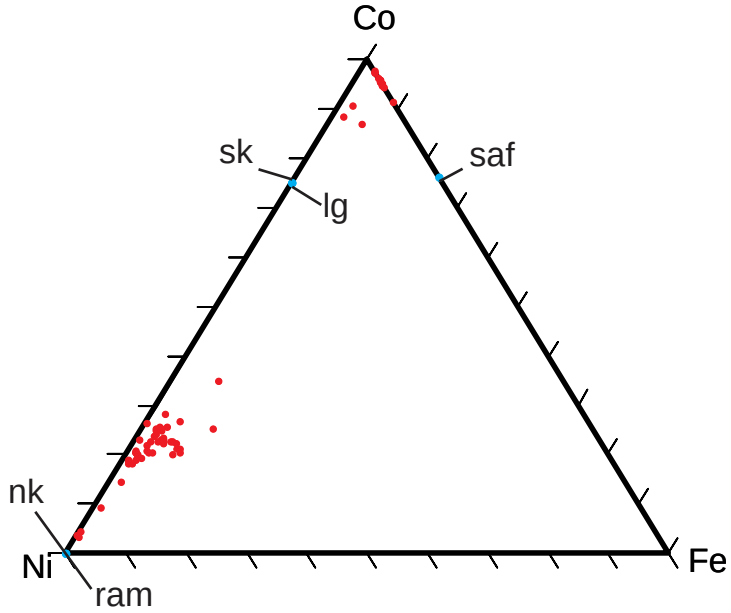

Figure 7: Arsenide ternary plots. ***including standard data points.** Distribution of endmember compositions between various data points corresponding with a), (Ni,Co)As, and b), (Ni,Co,Fe)As, found within the samples. *note not all analyses are present within these diagrams. Blue circles represent standards (data taken from webmineral data base), red represents data from our study. (sk=skutterudite, ram= rammelsbergite, lg=langisite, nk=nickeline and saf=safflorite).

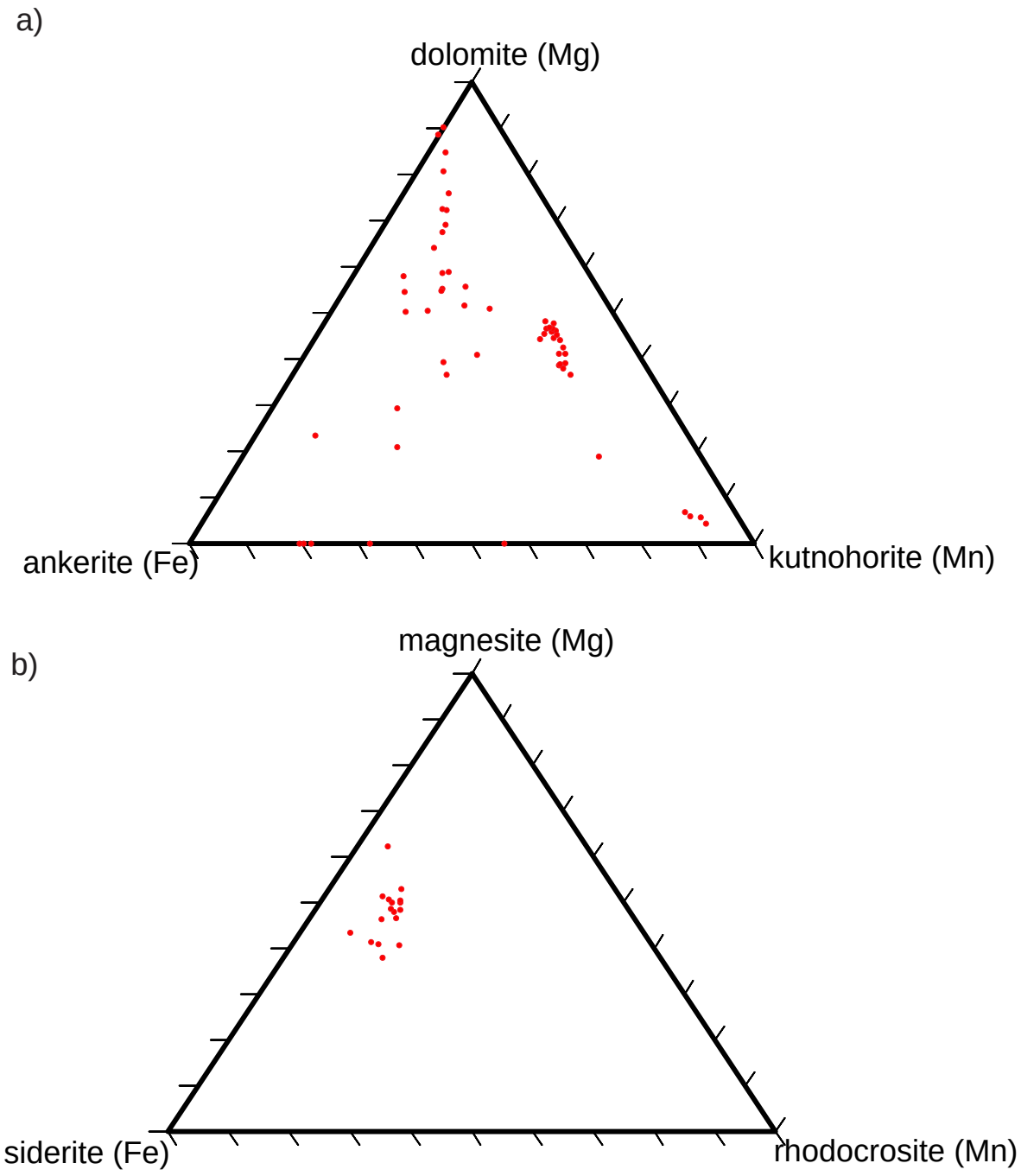

Figure 8: Ca-carbonate and ca-poor carbonate ternary diagrams. Diagrams show the distribution between Ca-rich carbonates a) and Ca poor carbonates b) between the Fe, Mg and Mn. Calcite is also found present but not visible on these diagrams. These diagrams do not contain all data points for this study.

langisite. Fig 7b illustrates the relationship between Ni, Co and Fe. We see an obvious lack in Fe within the arsenides, as the majority of analyses are near Ni or Co.

The carbonates in the system are Mg, Fe and/or Mn rich and either calcium-rich (such as dolomite, calcite, etc.) or calcium poor (siderite, etc.). Fig. 8a shows the calcium compositions from a portion of the samples and depict two groups. One group showing a composition placed between dolomite and kutnohorite (the magnesium and manganese endmembers respectively. The second group shows a movement from a mix of Mg and Fe-rich carbonates to dolomite. Fig. 8b shows the composition of a small portion of the calcium-poor carbonate samples, all of which have a similar composition between magnesite and siderite.

3.4 Uranium mineral chemistry

An advantage this study has over some of the older studies of the area is access to modern analytical techniques. One of these methods, LA-ICP-MS, has allowed us to accurately determine the trace elements present in the uranium phases of Port Radium. Spot analysis was done on three spatially distinct botryoidal occurrences. An element map was generated using laser ablation from one of these botryoidal areas to see if the composition varied within one depositional occurrence. Laser ablation was conducted solely on uranium phases and when possible, avoided areas containing arsenides. This is due to the effect of arsenic on the receptor as it contaminates it and has long washout times.

Primary uraninite examined in this study exhibits high $HREE_N/LREE_N$ ratios with slight negative Eu anomalies and variable Th contents (Fig. 9 and 10)

Fig. 10 and 11 show the chondrite normalized trace element patterns for both primary and secondary uranium occurrences. Based off the data for REEs and trace elements, all the primary uraninite data (brighter colours) show extremely similar trends in HREE composition and some variation within the LREEs. Their trace metal composition does vary (Fig. 10); some elements show orders of magnitude in differences such as Hf. Data points from one of the occurrences show a difference of 1 to 2 orders of magnitude in Ti concentrations when compared to the other samples.

**Table 4: Variations in the chemistry of uraninite and associated inclusions. ***inclusions in brackets indicate these are inclusion bearing zones

Sample	Site	Spectrum	Feature/Area	As	Ca	Co	Fe	Ni	Pb	O	S	U	Total
289-2	6	3	Inclusion	52.8		18.44		7.32			21.43		100
289-2	6	4	Inclusion	50.5		18.5	1.43	9.46			20.11		100
289-2	6	8	Inclusion	51.46		17.44	1.68	9.04			20.38		100
289-2	10	1	Inclusion	48.21		24.37		6.09			21.33		100
289-2	10	2	Inclusion	50.77		19.78	1.37	8.06			20.02		100
289-2	10	8	Inclusion	52.01		19.46	1.37	7.35			19.8		100
289-2	10	9	Inclusion	48.65		22.17		7.14			22.03		100
289-2	8	3	Rim (inclusions)		1.41				10.13	22.49		65.97	100
289-2	8	4	Rim (inclusions)		1.3				18.54	16.21		63.94	100
289-2	8	5	Rim (inclusions)		1.17				11.13	22.14		65.55	100
289-2	8	6	Rim (inclusions)		1.28				10.31	23.21		65.19	100
289-2	8	13	Barren		0.71				13.5	21.19		64.6	100
289-2	8	17	Barren		0.87				12.26	22.05		64.83	100
289-2	8	18	Barren		0.86				12.57	21.82		64.74	100
289-2	8	19	Barren		0.83				12.49	21.68		65.01	100
289-2	8	25	Core (inclusions)		1.1				10.87	22.3		65.74	100
289-2	8	28	Core (inclusions)		1.24				7.98	24.61		66.18	100
289-2	8	29	Core (inclusions)		1.12				10.89	22.57		65.42	100

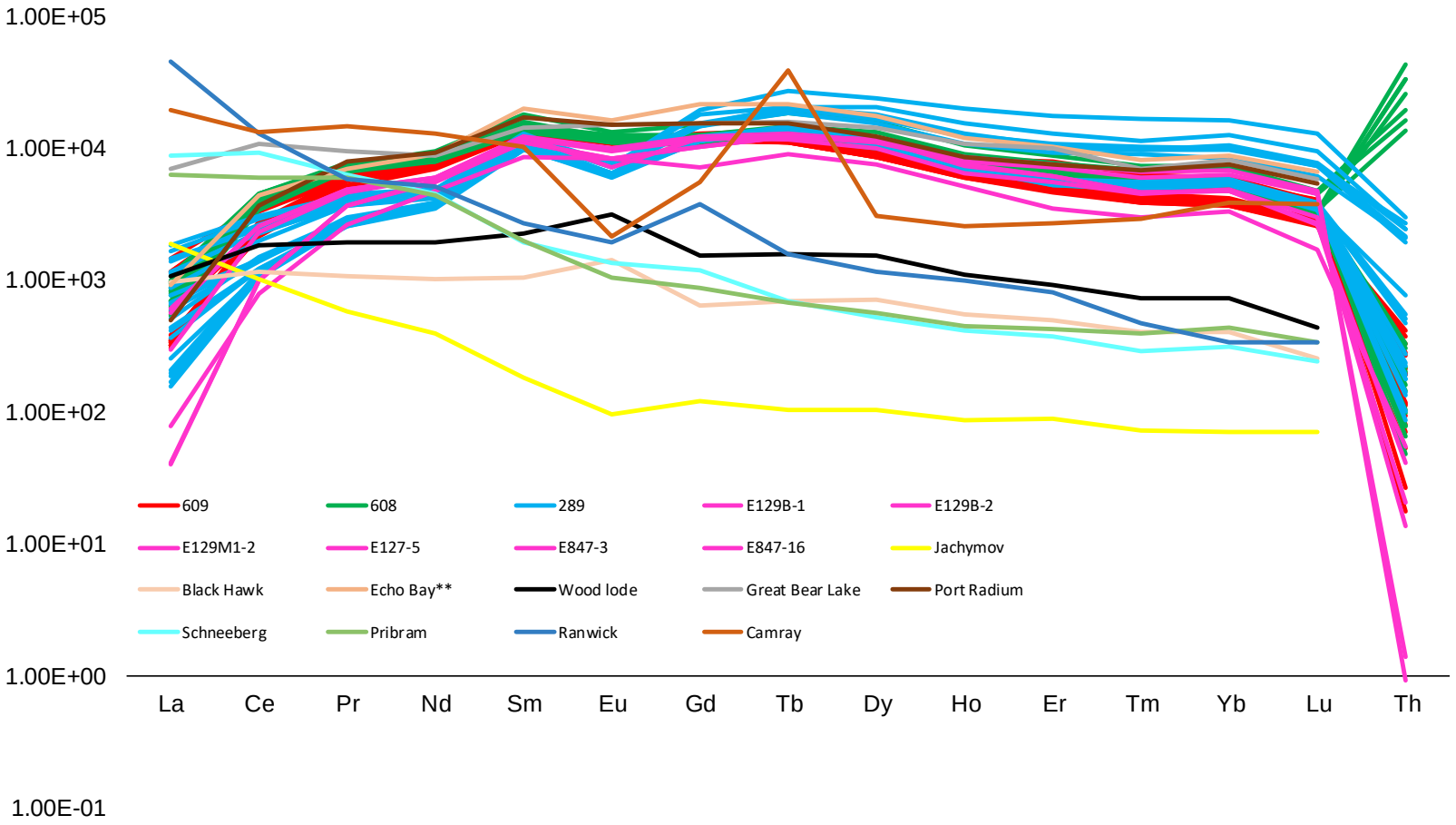

Figure 9: Spot analysis REE spider diagrams for world deposit: Comparison of our LA-ICPMS data of uraninite (samples 609, 608, 289) vs. samples reported by Gandhi et al. (2013) labelled as "E****" and samples reported by Alexandre et al. 201, consisting of uraninite samples from other uranium enriched five metal deposits around the world. Data sets from Alexandre et al. 2015 lacks thorium data. Value normalized to C1 chondrites, McDonough & Sun (1995).

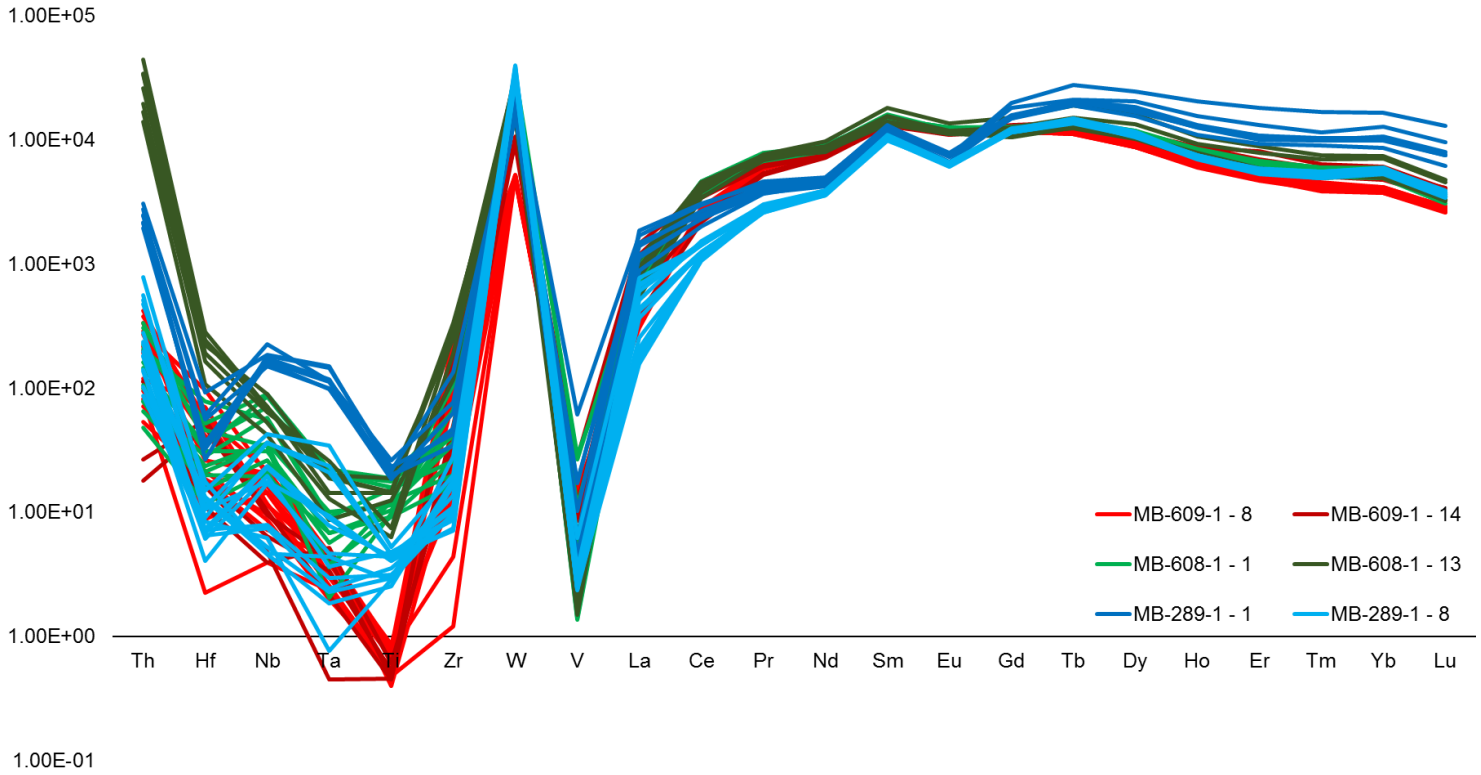

Figure 10: Spot analysis REE + trace metal spider diagrams of uraninite. Variations between primary and secondary occurrences of uraninite within our samples. Trace metals chosen due to their importance in distinguishing UO_2 and U_3O_8. Dark colours represent secondary occurrences. Values normalized to C1 Chondrites, McDonough & Sun (1995).

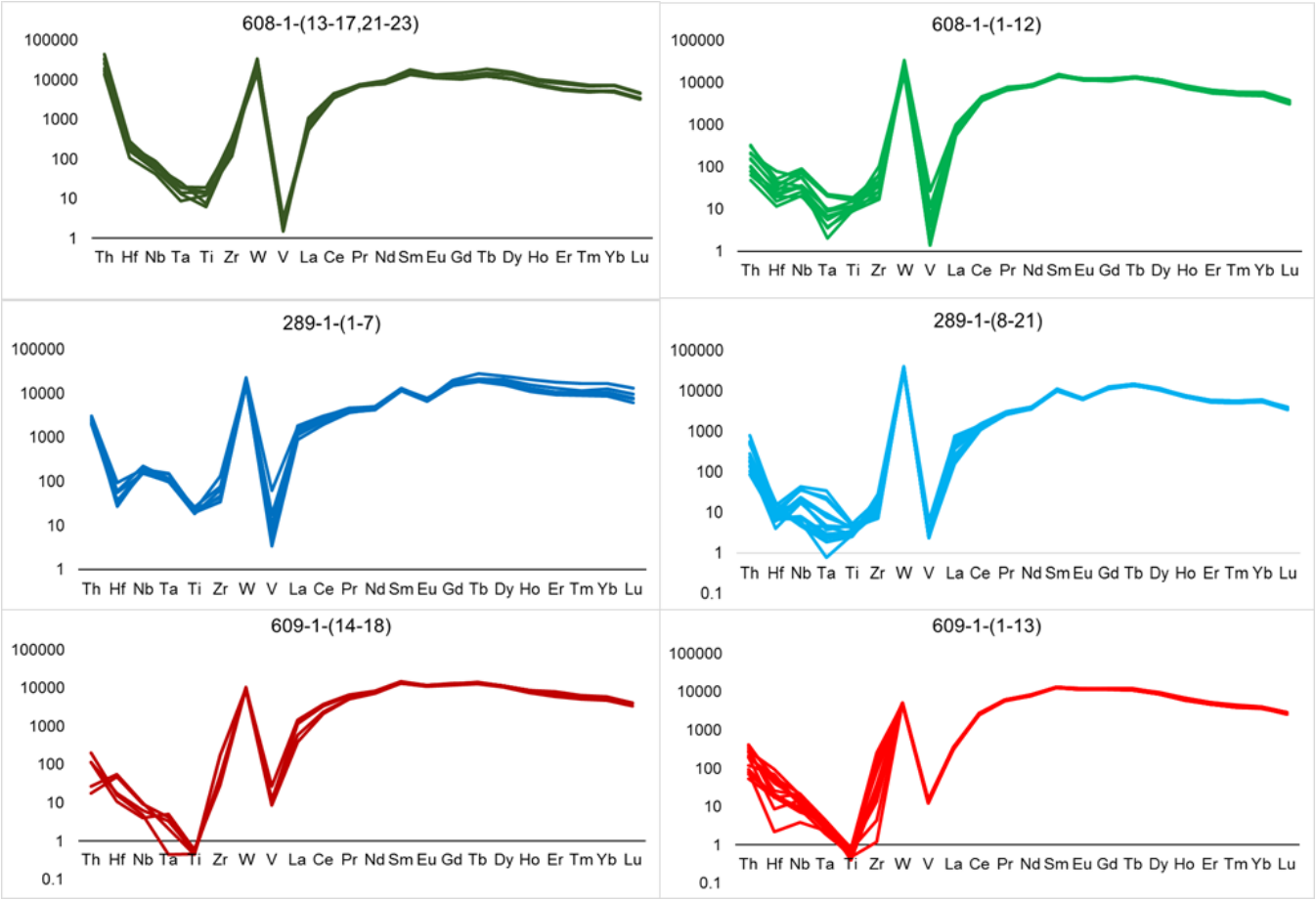

Figure 11: Breakdown of Figure 10 by sample and occurrence. Primary occurrences in bright colours, secondary in darker. Colours match Figure 9. Values normalized to C1 Chondrites, McDonough & Sun (1995).

The darker graphs in Fig 10 and 11 reflect trace element compositions of secondary uraninite occurrences. These uraninites show every similar REE patterns and concentrations to the primary uraninite found in their respective samples. One exception is the secondary uraninite in sample 289, which has consistently higher REE contents than the primary event, while following a similar trend. Compared to primary uraninite, secondary uraninite contains higher Th contents. The secondary uraninite in sample 289 shows higher Nb, Ti and Ta over its primary phase but follows the same trend.

Primary botryoidal uraninite is zoned, with alternating dark and light zones following its crystal habit. Dark areas were also observed along fractures. Darker zones contain 9-12 wt% Pb and 1-2 wt% Ca as opposed to brighter areas that contain 12-15% wt % Pb and less than 1 wt% Ca. Fig. 12 shows the distribution of these features and others. The darker areas that follow concentric growth zones are rich in inclusions of cobaltite (Fig. 13). The inclusions are ~ 1 to 10 μm in size, exhibit dendritic habit and are also distributed solely in the darker zones (Fig. 14). Table 4 shows the compositions of the inclusions and the variations in Pb and Ca content between them.

Laser ablation was conducted on large botryoidal section (Fig. 15). The element maps show that bright, inclusionless zones contain high Th, Hf and Zr, whereas the darker zones contain high Ti, Ta and Nb with low W, V and Sb. (Fig. 16). Metals such as Ag, As, Co, Ni, Mo and Ti as associated with the inclusions present within the dark zones.

Uraninite altered by coffinite in Fig. 3 was mapped using the SEM (Fig. 17). Coffinite shows very little variations in uranium contents compared to uraninite (Fig. 17c). Coffinite contains slightly higher silica which is most notable around the edges of the wall rock (Fig. 17b). The bright spots are associated with aluminosilicates within the gangue.

Later secondary occurrences of uranium have been noted, showing low U wt % (approx. 30%) and high O compared to all other occurrences of an uranium bearing mineral.

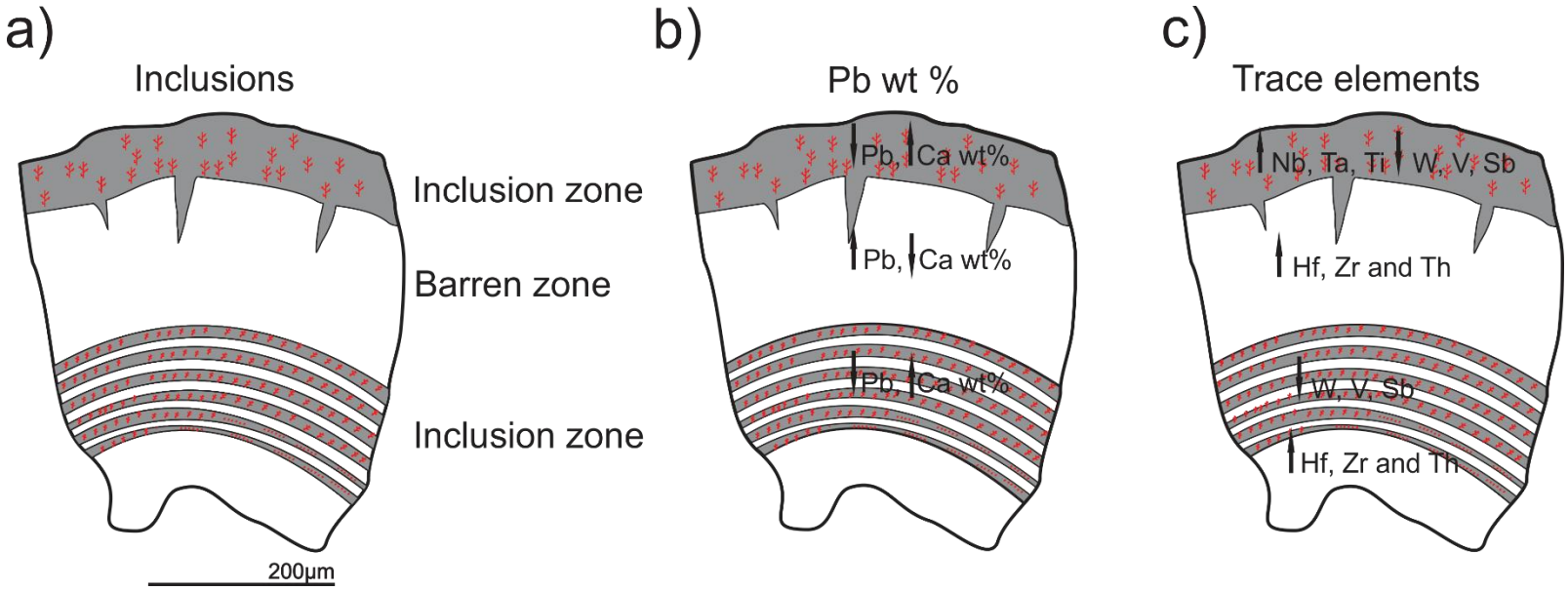

Figure 12: Variations in characteristics of the uraninite zones. Sketches indicates the various changes between the zonations in botryoidal uraninite. a) depicts physical differences. b) variations in Pb and Ca between the zones. c) shows the variations in trace elements between the zones (does not include trace elements associated purely with inclusions. These elements include: Ag, As, Co, Ni and Mo. The inclusions are not proportional in diagrams).

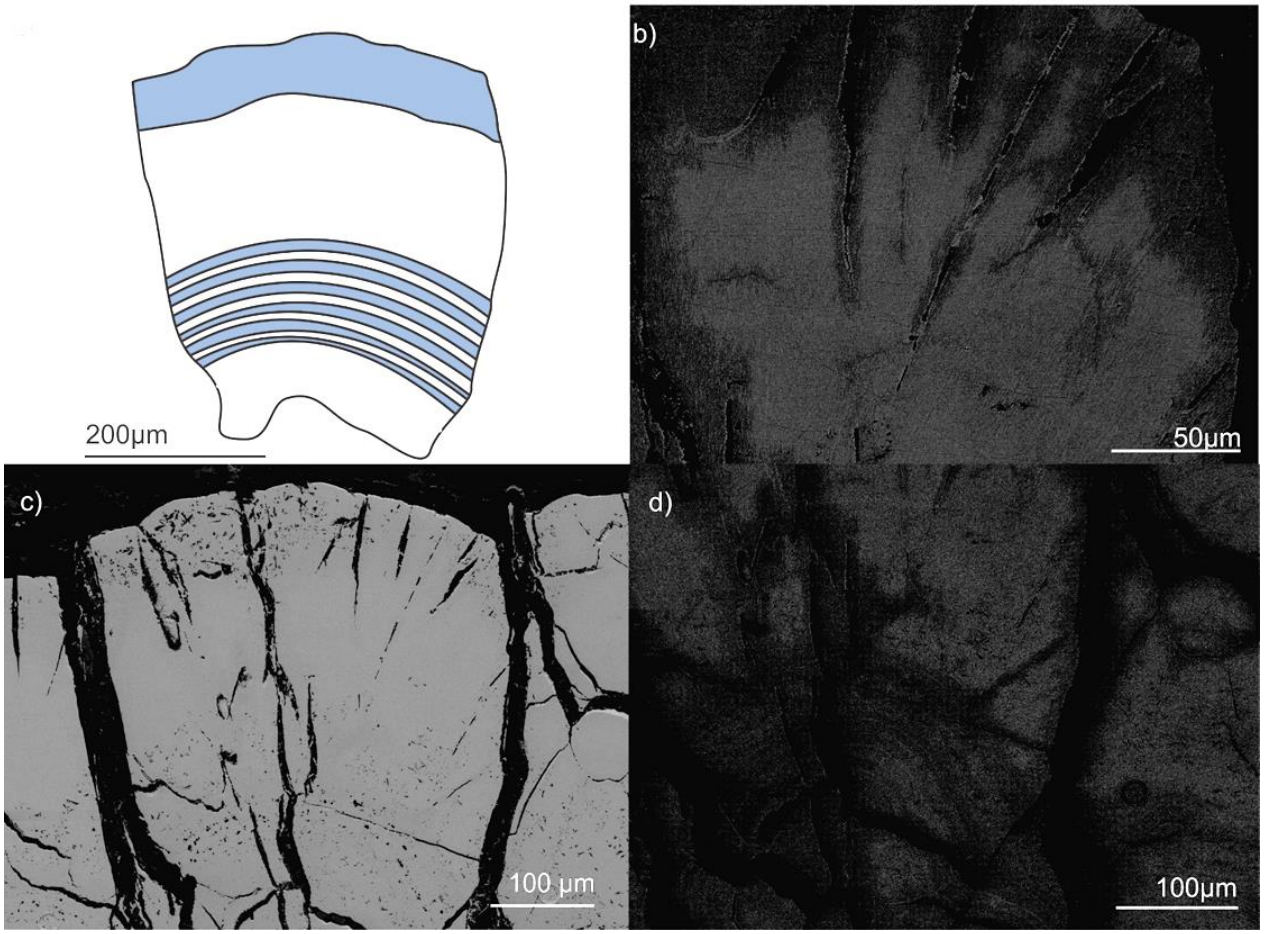

Figure 13: Inclusion zone sketch, natural and enhanced SEM BSE images. a) is a sketch of the botryoidal uraninite grain showing inclusion rich areas in blue. c) is the SEM BSE image of the area showing inclusions. b) and d) are enhanced SEM BSE images showing the density contrast (by shade differences) and inclusion zones/banding

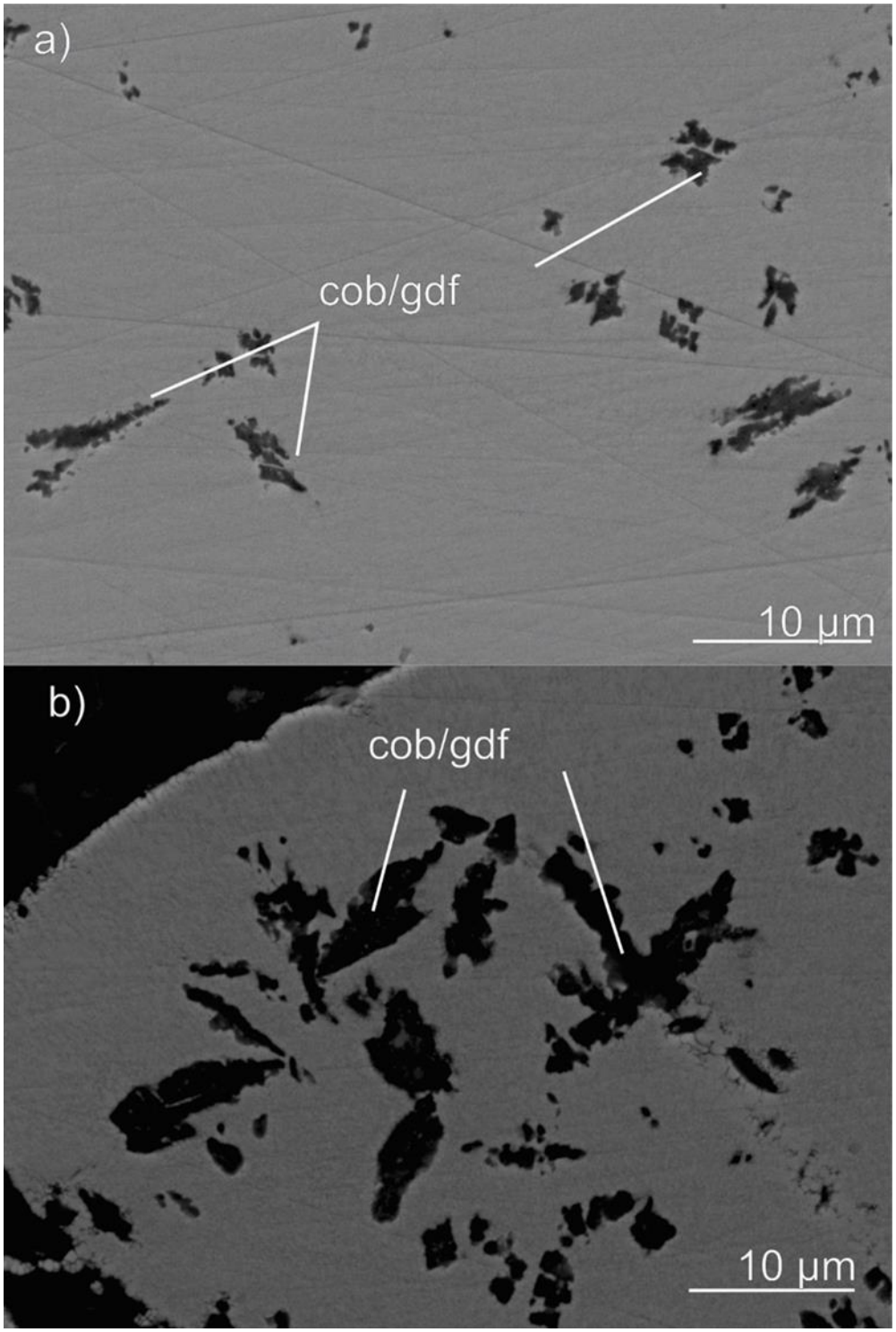

Figure 14: Inclusion shape and size. Close up of inclusion zones in uraninite showing shape and size of cobaltite inclusions. b) shows dendritic habit.

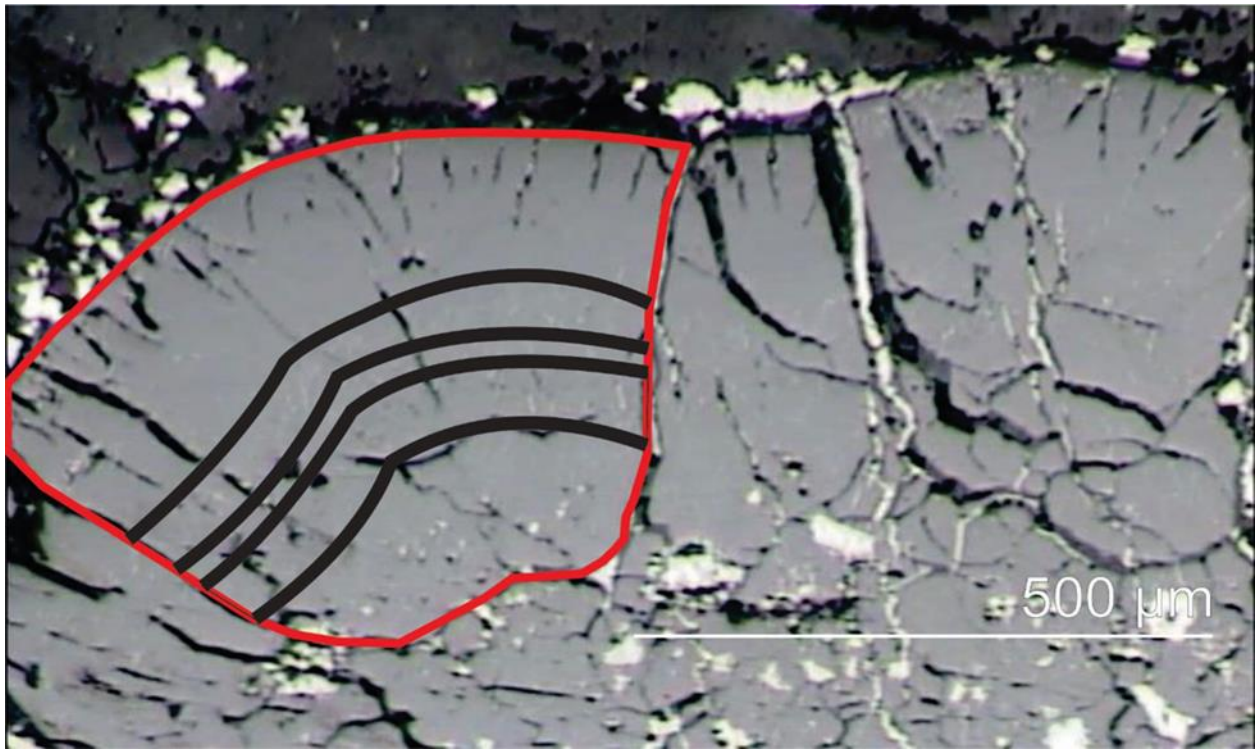

Figure 15: LA-ICPMS map location. *reflected light image. Red outline shows map boundaries, black lines outline the inclusion band.

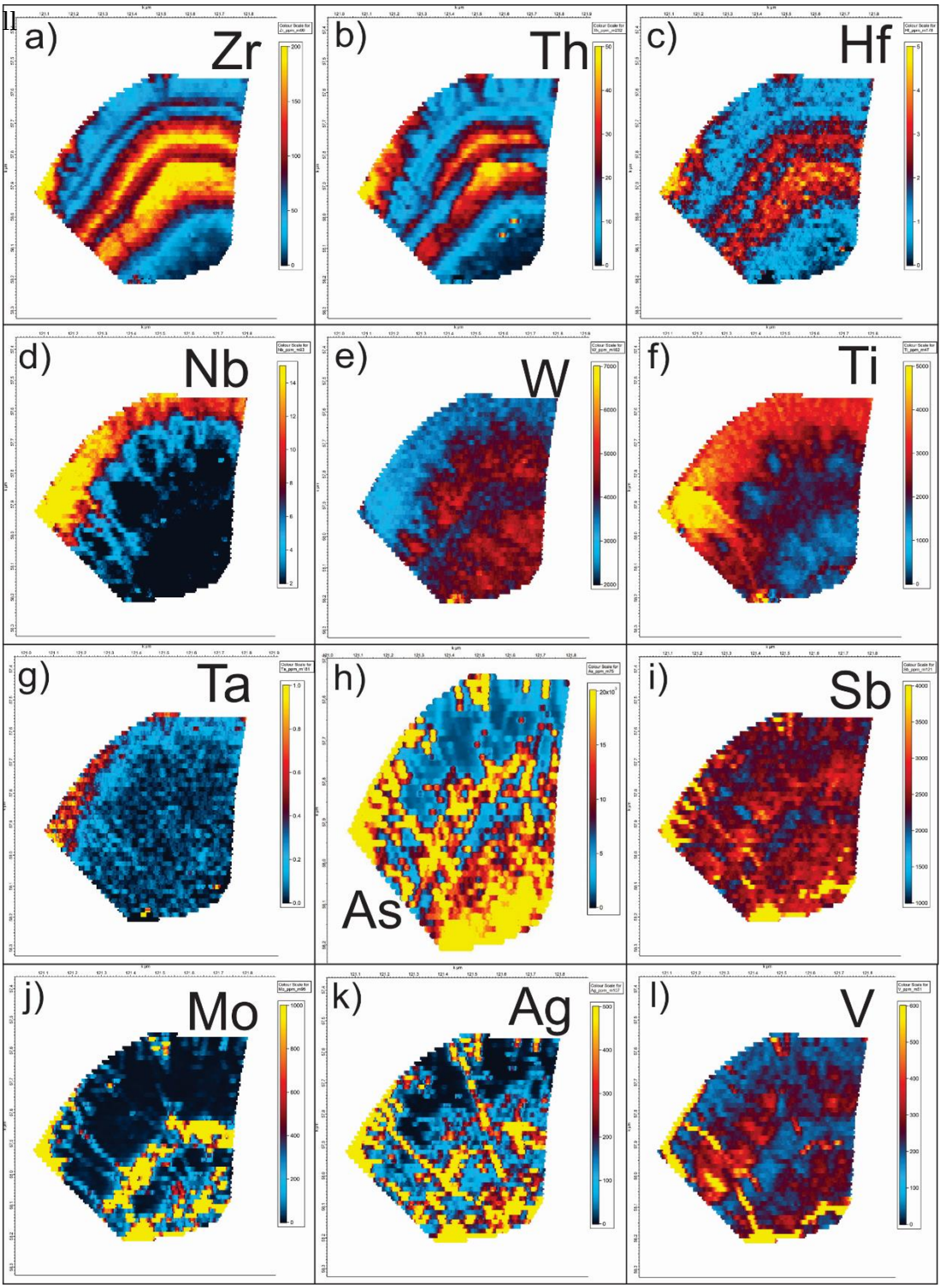

Figure 16: Trace element maps in botryoidal uraninite. Shows variation in REE and trace metals over a single precipitation event. Three distinct zones are visible; one with inclusions (Ag, As, Mo and Ti), one with barren zones (Zr, Hf and Th) and the last with (dark) inclusion rich zone (W, V, Ti, Nb and Ta).

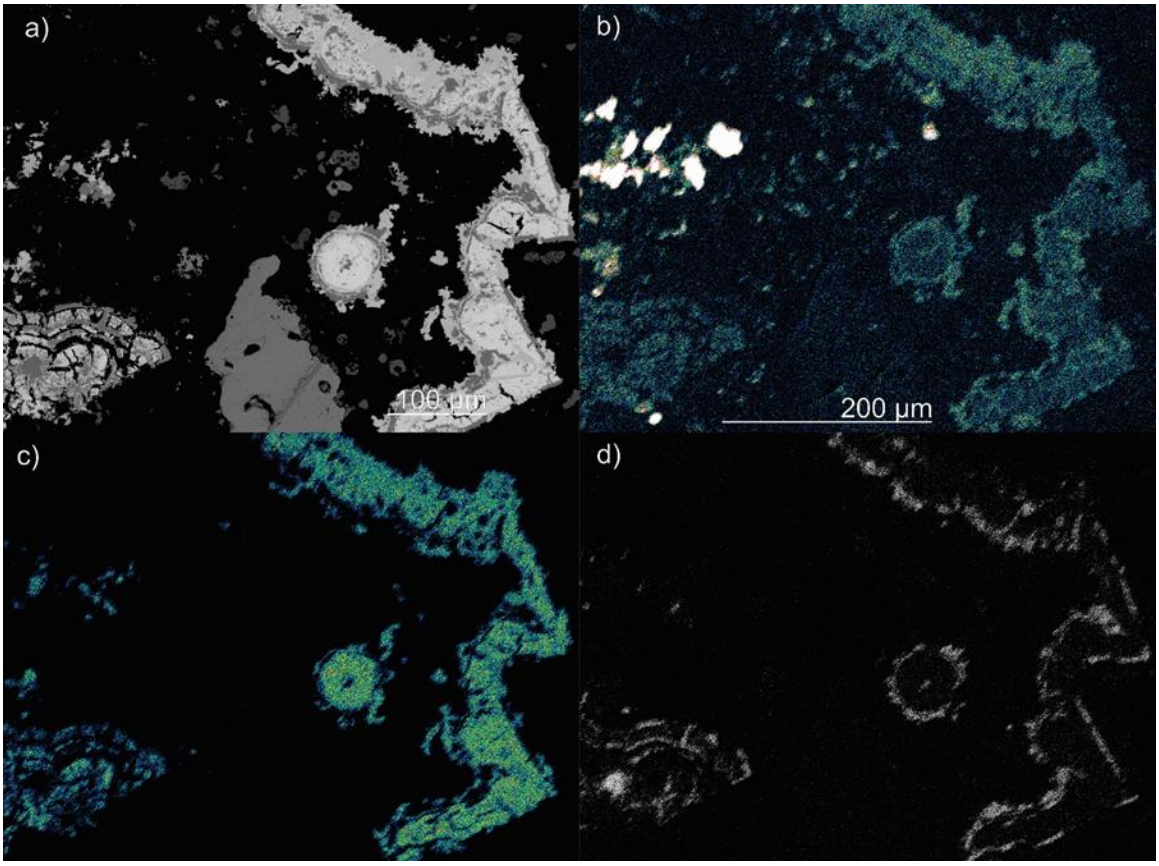

Figure 17: SEM element map for coffinite alteration of uraninite and sulpharsenide cycle. a) area map. b) Si map with bright spots indicating higher Si content associated with being an aluminosilicate. “Greener” border showing higher content of Si associated with coffinite. c) uranium map shows little variation between coffinite and uraninite areas. d) cobalt variation in cobaltite/gersdorfite.

The last variation of note, is the precipitation of the unknown uranium phase shown in Figure 6c. This phase was precipitated last and contains the lowest amount of uranium. Initial interpretation had this phase as betafite, however Raman spectroscopy results do not support this interpretation. Betafite has a singular diagnostic peak located at a wavelength of 893. Several other peaks are associated with it such as 601 and 657. The 601 and 657 wavelengths are associated with the TiO present in betafite, Fig. 18a shows the peaks associated with betafite, taken from Frost and Reddy (2010), while the data (Fig. 18b) lacks peaks associated with it.

4.0 Discussion

4.1 Paragenetic Sequence

4.1.1 Stage 1: uraninite ± sulfarsenide

Based on textural relationships found within our sample, the paragenetic model for Port Radium began with the crystallization of uraninite. Uraninite crystalizes as botryoidal uraninite, indicative of open space growth (Fig. 3a, b, c, and d). The uraninite is zoned into two distinct areas (interpreted as UO_2 and UO_2+U_3O_8) (Fig.13) with variations in:

- Pb and Ca wt% (UO_2 areas result in 12+ wt% Pb, and below 1 wt% Ca and the UO_2+U_3O_8 mixed zones show below 11 wt% Pb [one anomaly did exist within out data set{Table 4}] and 1+ wt % Ca)
- trace element composition (Hf, Th, Zr, Ta, Ti, W and Nb)
- the presence/absence of cobaltite inclusions

One zone lacks the cobaltite inclusions, contains higher Pb wt% concentrations and has an trace element composition containing the elements Hf, Th and Zr (Fig.16). This zone is representing uraninite in the form of UO_2. Uranium in the form UO_2 allows for only a 4^+, which is a charge supported by the dominant trace elements (Hf, Th and Zr) present in these areas. The increased Pb wt% (Table 4) is a result of the uraninite being in the form of UO_2. In this form, it has more U per unit formula than U_3O_8, which would

Table 5: **Updated Paragenetic sequence**, with uranium phases updated and silver uncertainties marked with dashed lines. Stage # based off Gandhi et al. (2013) model.

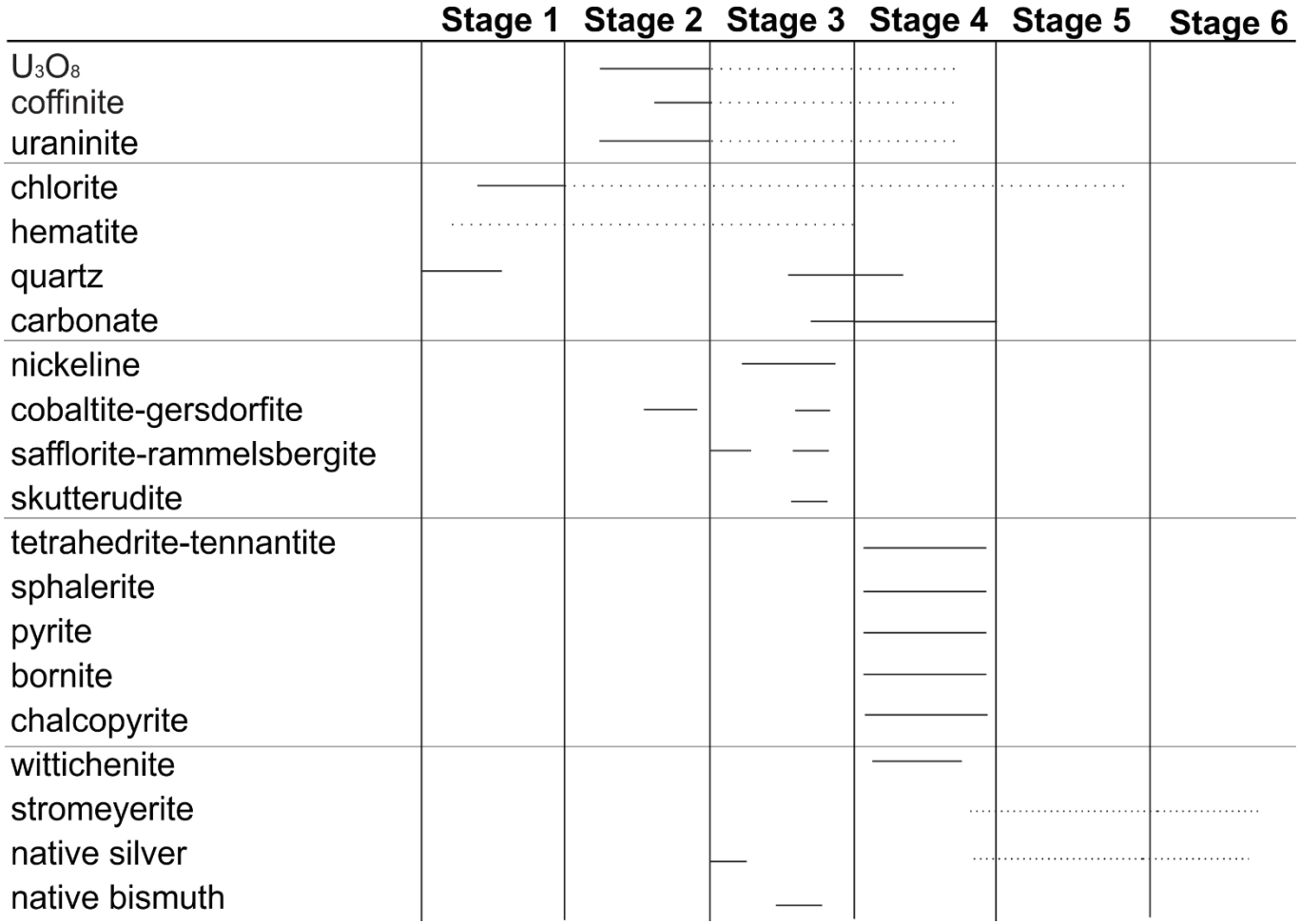

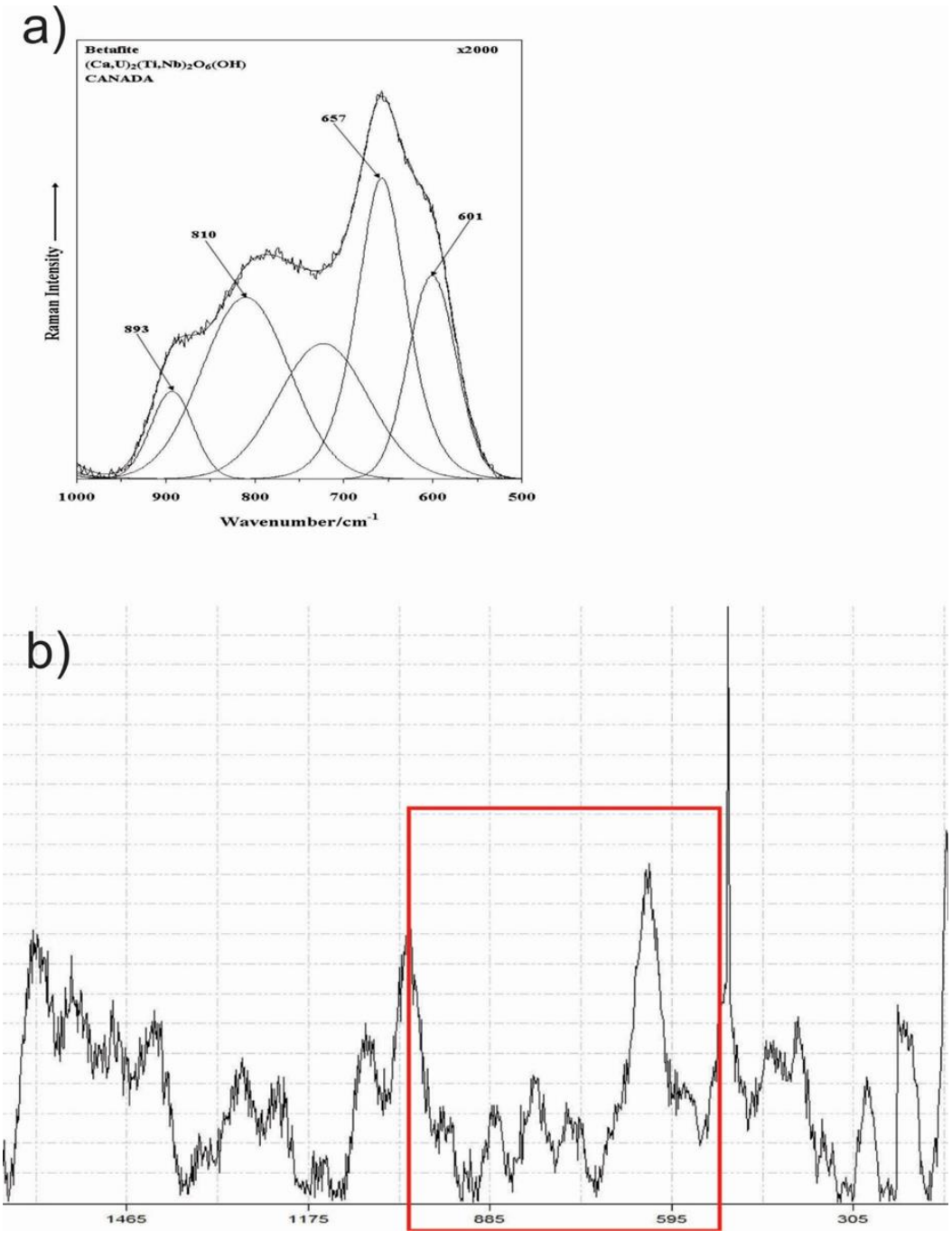

Figure 18: Raman data analysis of UUP. a) wavelengths/peaks associated with betafite. b) our spectrum and enclosed area is where peaks would be found, Frost and Reddy (2010).

Table 6: Paragenetic sequence of enhanced image (Fig. 13). Paragenetic sequence of primary botryoidal uraninite, denoting changes in trace element composition based on SEM enhanced images from Figure 13.

Sequence order	Mineral Stage	Inclusions	Banding	Enriched	Depleted
1*	U_3O_8	Yes	Yes	Inclu.	W, V
2	UO_2	No	No	Hf, Th and Zr	
3	U_3O_8	Yes	No	Inclu.	W, V**
4***	U_3O_8	Yes	No	Ti, Ta, Nb	W,V

* Indicates the first distinctive visible layer, earlier barren zones do exist.

** Present in the area, most likely due to overprinting

*** This stage is alteration of the previous stage by later fluid circulation

produce more Pb as it decays through time.This interpretation assumes that all Pb has been the result of radioactive decay and that no reprecipitation of the uraninite has occurred. The Ca wt% in these zones were all below 1 wt%, no explanation has been found by this study.

The second zone seen is the zones with the inclusions. The uraninite in these zones are interpreted as a mix of UO_2 and U_3O_8. The presence of UO_2 in these zones can explain the presence of the Ti and W as their charges are all 4^+ while the presence of U_3O_8 could explain the Nb and Ta with the $5^+/6^+$ charges. It can also explain the lower Pb content as it contains less Pb due to it having less U per unit formula. The trace elements associated with this zone have the charges 4^+,5^+ and 6^+. We see an inverse relationship (Fig. 16) present between W and Ti, both have a charge of 4^+. We see a depletion in V in these inclusions bearing zones and an enrichment in Nb and Ta. The depletions in the middle of the grain of W and V are interpreted to be primary depletions as they are present in the center of the grain in a uniform band where as the W/Ti relationship and the Nb, Ta enrichments in the appear to be the result of later circulating fluids as they follow fractures within the grain. These areas showed Ca wt % values above 1 wt%, once again, no explanation can be given. The uraninite has been described to show two different relationships with the sulfarsenides: as inclusions as well as bands within uraninite (Fig 14 and 4 respectively). It is unknown if these occurrences are precipitated from the exact same event. The uraninite associated with the sulfarsenide bands are noted to have Si present within its structure and is seen being altered to coffinite (Fig. 17b), while the uraninite with the inclusions lacks this association with Si.

The inclusions are cobaltite in composition and are of primary origin as they are not restricted along fracture zones or show evidence to be precipitated with remobilised uraninite. There are two possibilities of primary formation of these inclusions, they are either the result of exsolution crystallization or are coeval. These inclusions display a texture interpreted to be dendritic texture (Fig. 14), which is indicative of open space growth. This indicates that the sulfarsenide inclusions co-precipitated with the uraninite. There is a trace element composition associated with these sulfarsenides (Fig. 16) showing enrichments in Ti, As, Mo and Ag as well as a depletion in Sb.

4.1.2 Stage 2: arsenides ± Ag, Bi

This stage begins with the precipitation of Ag dendrites. The Ag precipitation has been in two different styles; once where silver was precipitated continuously until it was followed by the formation of an arsenide shell (Fig. 5d), or there as an alternation between Ag and an arsenide (Fig. 5a) creating multiple thin layers of each metal, then moves into the formation of the arsenide shell. As the arsenide dendrites grow, their composition becomes more Ni rich until they reach either a NiAs (nickeline) or $NiAs_2$ (rammelsbergite) composition before their formation stops.

In some instances, a brief period of sulphur enrichment is visible around the rim of these dendrites. This enrichment indicated by the abrupt change to a darker coloration of the dendrite SEM images around the edge (Fig. 5d and 5e).

After the formation of the dendrites, they are later intruded by native Bi (Fig. 5e and 5d) which replaces the Ag cores of the arsenide dendrites. This occurs after the full formation of the dendrite as we can see small fractures cutting across the dendrite leaves, but it occurs before the emplacement of the gangue minerals as the fractures halt at the interaction between the gangue and dendrite (Fig. 5d).

4.1.3 Stage 3: sulphide ± U, Ag and carbonate

Sulphides are found disseminated in both the wall rock as well as in later forming carbonate. Chalcopyrite is the dominant sulphide found disseminated in carbonate or in conjunction with bornite showing box work texture (Fig.6b and 6e). Other sulphides found include: sphalerite, pyrite, wittichenite (Cu_3BiS_3) and tetrahedrite-tennantite.

A late U phases, native Ag and stromeyerite (AgCuS) occur with the carbonate-hosted sulfides. These minerals occur as an irregular zoned anhedral mass with Uup at the core, mantled by stromeyerite and rimmed by Ag (Fig. 6c). Native Ag and stromeyerite also occurs along the rim of a bornite chalcopyrite grains (Fig. 6a).

The carbonates within our system can be divided into two main groups; Ca-rich and Ca-poor (Fig 8). The carbonates produced were dolomite, ankerite, kuthnorhorite, magnesite, rhodochrosite, siderite and caclite. Each group is comprised of the same three

Table 7: Uranium phases. Sample list of variations between uranium phases present in study.

Mineral	Sample	Site	Spectrum	Al	As	Ca	Cl	Cu	Fe	Mn	Pb	O	Si	Ti	U	Y	Total
High Ti/O uranium phase	608-2	12	2			1.38			1.31			42.62	2.09	17.63	33.1	1.86	99.99
coffinite	704-1	4	5		2.43					0.83		31.56	4.01		61.17		100
uraninite	289-2 Thick	2	2			1.27					10.66	22.43			65.64		100
unknown uranium phase	843	4	8	0.28		1.09	0.38	7.96	3.65			44.76	1.36	33.54	6.99		100.01

endmembers; Fe, Mg and Mn. Two trends were noted in their composition; the Ca-rich contains a group of Mg-Mn rich carbonate and a Ca-poor trend of Fe-Mg composition. The carbonates can be seen interacting with multiple phases, such as infilling cores of the dendrites (Fig. 5c) or carrying the sulphides.

4.2 Comparisons to previous models

The reduction from 5+ stages to our three stages model occurred due to lack of textural evidence of the presence of several stages as well as the overlap of precipitation not previously mentioned in literature.

The first stage mentioned in the Gandhi et al. model (Table 2) is the barren quartz stage. This stage is absent from our model due to the lack of textural evidence. Within our samples, there exists large, euhedral grains of quartz, however there is no textural relationship between it and another phase to confidently say it is the *Stage 1: barren quartz* . The barren carbonate stage as well, could not be confidently identified in sample.

The final stage in the Gandhi et al. (2013) has been amalgamated with the sulphide bearing stage as native Ag has been associated with an Ag-sulphide in all instances within our samples (outside of our Stage 2 occurrences). Using the stages of the Gandhi model, this relationship between native Ag and stromeyerite either extends the precipitation of the sulphides into their Stage 6 or allows for the precipitation of native Ag earlier than their stage 6. The presence of native Ag with the sulphides led to the combination of the Stage 4 and 6 of the Gandhi model.

The uraninite within our samples displays a high $HREE_N/LREE_N$ ratio (Fig. 10) and displays similarities only with 2 grouping of samples when compared to sites from around the world (Fig.9). The only samples to produce values similar too ours were the samples from the Gandhi et al. (2013) study of Port Radium as well as the GBL occurrence from the Alexandre et al. (2015) study. This GBL occurrence shows an enrichment in Ce and La, as well it lacks the negative Eu anomaly that our samples display (Fig.10).

4.3 Implications

The change within the individual uraninite grains from UO_2 to U_3O_8 can likely be attributed to a slight increase in fO_2, such that the oxidation state changes from a 4^+ to a $5^+/6^+$ mix while still allowing for uraninite to precipitate. The role of pH on the chemistry of the uraninite is unclear.

The overlap of the arsenides into the uranium phase is shown by the inclusions of cobaltite within the uraninite grains. Arsenides require conditions of low fO_2 and varying pH levels to precipitate (see appendix, Markl et al. 2016). These inclusions coincide with the U_3O_8 enriched zones within the uraninite. These inclusions are more likely the result of coeval precipitation as the inclusions are portraying dendritic texture which is an open growth texture. The other possibility is exsolution crystallization, however this is unlikely as this would not result in dendritic texture. We see a change in composition of arsenides and sulfarsenides as we move from these inclusions into the arsenide stage, Co to a more Ni rich composition. Based off the phase diagrams shown in Markl et al., (2016) (see appendix) this change results from a decrease in pH and require low fO_2.

A mixing of fluids is a possible candidate to explain the relationships found within this study, however the exact mechanism for precipitation is unknown and can only be speculated as the mechanisms which force these phases (U_3O_8 and arsenides) are opposite (increase in fO_2 and low fO_2 respectfully) and the purpose of this study was focused on paragenetic sequence and

The very last stage of mineralization within the polymetallic model is native silver. With the same phase diagrams from the Markl et al., (2016) paper, we see that to precipitate native silver within these systems we need a shift back to more neutral levels of pH as well as an increase in fO_2 to precipitate the native Ag.

Our study indicates that the genesis of the polymetallic system at Port Radium required a widely varying set of parameters it to precipitate. Future areas of study of this environment could be analysis of the stable isotopes of uraninite to determine the fluid source based off the isotope values of oxygen. Another area may be to determine the source of the metals whether it be from a sedimentary basin or bitumen.

5.0 References:

Alexandre, P., Kyser, K., Layton-Matthews, D. and Joy, B., 2015, Chemical compositions of natural uraninite, The Canadian Mineralogist, v. 53, p. 595-622.

Campbell, D.D., 1955, Geology of the pitchblende deposits of Port Radium, Great Bear Lake, Northwest Territories: Unpublished Ph.D. thesis, Berkeley, U.S.A., California Institute of Technology, 323 p.

Changkakoti, A., Morton, R.D. and Gray, J., 1986a, Hydrothermal environments during the genesis of silver deposits in the Northwest Territories of Canada: Evidence from fluid inclusions: Mineralium Deposita, v. 21, p. 63-69.

Corriveau, L., Montreuil, J. and Potter, E.G., 2016, Alteration Facies Linkages Among Iron Oxide Copper-Gold, Iron Oxide-Apatite, and Affiliated Deposits in the Great Bear Magmatic Zone, Northwest Territories, Canada: Economic Geology, v. 111, p. 2045-2072.

Frost, R. L. and Reddy, B. J, 2010, Raman spectroscopic study of the uranyl titanate mineral betafite (Ca,U)2(Ti,Nb)2O6(OH)-Effect of metamictization, Radiation Effects and Defects in Solids, v. 165(11), p 868-875.

Gandhi, S.S., Potter, E. and Fayek, M., New Constrains on genesis of the polymetallic veins at Port Radium, Great Bear Lake, Northwest Canadian Shield. (Unpublished paper 26 p).

Gandhi, S.S., Potter, E. and Fayek, M., 2013, Polymetallic U-Ag veins at Port Radium, Great Bear magmatic zone, Canada: main botryoidal pitchblende stage cuts 1.74 Ga diabase dykes and has REE signatures diagnostic of unconformity-type deposits: Geological Survey of Canada, Open File 749_3, poster.

Jory, L.T., 1964, Mineralogical and isotopic relations in the Port Radium pitchblende deposit, Great Bear Lake, Canada: Ph.D. thesis, Pasadena, California, California Institute of Technology, 290 p.

Kidd, D.F. and Haycock, M.H., 1935, Mineragraphy of the Ores of Great Bear Lake: Bulletin of the Geological Society of America, v. 46, p. 879-960.

Kissin, S.A., 1992, Five-element (Ni-Co-As-Ag-Bi) Veins: Journal of the Geological Association of Canada, v. 19, p. 11$_3$-124.

Mercadier, J., Cuney M., Lach, P., Boiron, M.C.Bonhoure, J., Richard, A., Leisen, M., and Kister, P., 2011, Origin of uranium deposits revealed by their rare earth element signature, Terra Nova, v. 23.,p. 264-269

Markl, G., Burisch, M. and Neumann, U. 2016. Natural fracking and the genesis of five-element veins, Mineralium Deposita

Reardon, N.C., 1992, Altered rocks and magnetite-apatite-actinolite deposits associated with the mystery island intrusive suite, Echo Bay, district of Mackenzie. Mystery Island intrusive suite final report. Geological Survey of Canada, Open file 2506, p 62

Silke, R, 2009, The operational history of mining in the Northwest Territories,

6.0 Acknowledgements

I would like to take this time to thank several individuals for their help and input through this entire process. First off, I would like to thank Dr. Jacob Hanley (Saint Mary's University) for his tutelage and taking me on as an honours student for the past year. His mentorship has formed the basis of my geological career. Secondly, I would like to thank Dr. Erin Adlakha (Saint Mary's University) for her input in conversations, for her help in editing throughout the writing process. Without her this project would not be the same. The third individual I would like to thank is Corwin Trottier, MSc candidate (Saint Mary's University). I consider the time he took to listen to my ideas, provide feedback and constructive criticism to be invaluable. I would also like to thank the Geological Society of Canada and its TGI-5 association for funding the project and providing samples.

And Wilson.

7.0 Appendix:

Laser Ablation data, spot analysis. Sample 609-1. Normalized to C1 chondrites

Values (ppm)	Th	Hf	Nb	Ta	Ti	Zr	W	V	La	Ce	Pr	Nd	Sm	Eu	Gd	Tb	Dy	Ho	Er	Tm	Yb	Lu
MB-609-1 - 1	192.8	8.74	14.54	3.90	0.76	4.40	5065	13.88	338	2680	6261	8063	13149	11705	11402	11219	8736	6101	4800	3874	3733	2604
MB-609-1 - 2	269.7	26.02	20.42	4.04	0.87	32.98	5000	13.50	350	2821	6282	8381	13338	12202	11936	11690	9256	6648	4975	4045	4006	2824
MB-609-1 - 3	333.4	16.99	21.88	4.63	0.83	13.48	5065	15.38	358	2737	6261	8053	13547	12238	12309	12244	9472	6868	5338	4348	4124	2904
MB-609-1 - 4	378.6	57.38	21.83	4.04	0.83	80.63	4828	12.86	328	2602	5894	7834	12824	11492	11686	11163	8780	6154	4819	4081	3876	2644
MB-609-1 - 5	216.6	41.26	16.17	4.41	0.65	93.72	5000	12.52	348	2504	5981	8096	13277	11865	12500	12022	9691	6996	5394	4571	4174	2900
MB-609-1 - 6	118.6	69.81	11.71	2.57	0.52	194.24	5226	12.05	340	2564	5959	7987	12959	11581	11740	11884	9366	6612	5238	4377	4012	2928
MB-609-1 - 7	53.1	18.25	7.25	4.41	0.40	24.08	5065	12.79	320	2489	5819	7834	13527	12025	11490	11496	8789	6245	4919	4024	3845	2700
MB-609-1 - 8	193.8	57.28	11.46	4.34	0.65	133.51	4978	14.38	326	2635	6013	8009	13405	11918	11917	11385	8793	6465	4850	3988	3826	2648
MB-609-1 - 9	71.0	21.46	8.63	1.99	0.56	38.25	4903	13.80	305	2571	6088	8228	13385	12078	11686	11191	8744	5993	4700	3955	3727	2656
MB-609-1 - 10	81.4	2.25	3.92	2.35	0.48	1.20	5129	14.77	326	2595	6121	8293	13378	11705	11882	11413	9037	6227	4869	4170	3963	2804
MB-609-1 - 11	95.2	18.54	9.63	3.01	0.68	17.04	5129	14.29	351	2705	6282	8140	13520	11794	12029	11801	9264	6703	5013	4227	3888	2872
MB-609-1 - 12	286.2	97.09	20.13	3.09	0.80	256.54	4753	14.38	356	2618	5916	7965	13000	11421	11853	11828	9252	6557	5175	4211	3814	2696
MB-609-1 - 13	418.3	49.22	14.38	3.01	0.75	103.66	5194	14.18	344	2638	6272	8271	13122	11936	11971	11745	9232	6648	5113	4093	3901	2692
MB-609-1 - 14	112.1	17.57	6.38	3.38	0.52	39.32	10645	9.16	1177	3564	6121	7834	13486	11723	12647	13767	11260	8755	6969	5911	5571	4104
MB-609-1 - 15	114.8	10.97	3.96	5.15	0.61	29.32	9849	27.32	1456	3752	6606	8271	14662	11847	12745	14266	11382	8535	8063	6356	6025	4044
MB-609-1 - 16	200.7	16.02	4.79	0.45	0.45	50.52	9860	11.54	1177	3393	6099	7374	13243	11421	12647	13657	11138	8388	6788	5611	5180	4072
MB-609-1 - 17	18.0	48.35	9.46	4.26	0.47	171.99	9172	8.54	388	2152	5172	7133	12953	10906	11853	12659	10402	7564	6006	5053	4776	3404
MB-609-1 - 18	26.6	55.34	10.17	2.13	0.45	171.99	9849	11.96	588	2377	5377	7418	13770	11812	13039	13767	11382	8663	6594	5781	5137	3844

Laser Ablation data, spot analysis. Sample 608-1. Normalized to C1 Chondrites.

Values (ppm)	Th	Hf	Nb	Ta	Ti	Zr	W	V	La	Ce	Pr	Nd	Sm	Eu	Gd	Tb	Dy	Ho	Er	Tm	Yb	Lu
MB-608-1 - 1	160.7	30.97	31.21	6.84	10.45	47.64	21624	1.84	692	3850	7015	9147	14797	12611	12696	14100	11829	8462	6706	5955	5925	3744
MB-608-1 - 2	304.1	52.04	89.58	22.28	18.73	64.92	15968	2.00	786	4176	7091	9081	14730	11616	11765	13518	10935	7894	6269	5405	5491	3312
MB-608-1 - 3	99.0	23.69	36.25	10.07	11.45	35.34	23226	11.25	886	4029	6713	8118	14595	11208	11667	12825	10447	7234	5763	5049	4913	3084
MB-608-1 - 4	47.9	11.75	20.88	3.82	9.16	16.75	29677	28.57	692	3980	7252	8687	14797	12558	11618	13269	11626	7912	6719	5943	5658	3824
MB-608-1 - 5	65.2	19.90	19.50	6.76	9.23	26.13	24409	1.37	550	3719	6918	8184	13919	11847	11324	13324	11138	7912	6206	5830	5516	3472
MB-608-1 - 6	334.5	37.77	70.42	20.59	15.84	41.62	20409	6.43	979	4620	7651	8687	14196	11936	12157	13186	10642	7839	6156	5352	5391	3516
MB-608-1 - 7	221.4	45.63	34.04	2.06	9.75	67.02	28817	6.07	844	4160	7101	8359	14459	12131	11422	13269	10976	7784	6206	5522	5366	3464
MB-608-1 - 8	205.5	78.45	56.25	8.82	12.11	106.28	21946	3.84	706	4144	7425	9037	14865	11901	12549	13961	11504	8297	6400	5522	5683	3604
MB-608-1 - 9	145.9	34.47	85.42	20.15	17.80	45.55	18688	5.54	975	4339	7543	8534	14459	11616	10750	12825	10569	7363	5631	5182	5019	3268
MB-608-1 - 10	78.3	28.16	57.42	9.26	15.39	25.65	24516	1.93	886	4160	7123	8249	14595	11705	11324	13019	10285	7546	5944	5575	5640	3364
MB-608-1 - 11	77.9	15.53	26.25	5.66	11.93	36.39	33978	26.79	996	4600	7845	8862	16081	11989	12010	13712	11789	7857	6500	5247	5217	3296
MB-608-1 - 12	105.9	21.17	34.75	3.60	12.20	19.90	23118	1.40	649	3834	7198	8556	14392	12185	11765	13213	11585	7619	6356	5984	5764	3636
MB-608-1 - 13	33551.7	222.33	90.00	20.00	18.86	252.88	14968	1.64	1089	4519	7500	8840	15473	11652	11176	13241	10366	7564	5869	5300	5087	3260
MB-608-1 - 14	34069.0	243.69	71.25	14.34	14.25	285.86	31828	1.99	785	4127	7284	8009	13919	11279	10539	12548	10488	7015	5481	4899	5205	3228
MB-608-1 - 15	43896.6	285.44	70.00	19.26	14.59	311.52	25344	1.81	945	4356	7543	8534	13966	11581	11387	12992	10744	7802	5875	5368	5211	3320
MB-608-1 - 16	13931.0	106.80	41.67	8.60	12.43	118.06	34624	2.56	823	4093	7112	8074	13365	11172	10980	12465	10366	7271	5750	5304	5261	3456
MB-608-1 - 17	26172.4	235.92	68.75	18.90	14.48	336.65	20161	1.49	835	4241	7026	8315	13986	11172	11324	12271	10163	7161	5681	5304	4919	3252
MB-608-1 - 22	16620.7	163.11	52.42	12.94	6.27	191.10	31075	2.27	541	3431	6886	8359	15243	11758	12632	15069	13293	9231	7825	6947	7068	4536
MB-608-1 - 23	19620.7	190.29	64.58	25.74	7.50	265.71	31398	3.14	629	3785	7619	9716	18108	13464	15147	18809	15894	10549	8825	7441	7379	4764

Laser Ablation data, Sample 289-1. Normalized to C1 Chondrites

Values (ppm)	Th	Hf	Nb	Ta	Ti	Zr	W	V	La	Ce	Pr	Nd	Sm	Eu	Gd	Tb	Dy	Ho	Er	Tm	Yb	Lu
MB-289-1 - 1	2472.4	60.19	225.00	114.71	26.36	77.49	22903	61.61	1692	2985	4612	4967	12770	7407	18186	20997	20528	15513	13125	11498	12671	9520
MB-289-1 - 2	1941.4	35.83	164.17	111.76	18.98	47.54	17226	3.34	882	1990	3690	4381	11926	7282	14853	20028	17033	12473	10313	9960	10043	7480
MB-289-1 - 3	3065.5	92.23	186.25	150.74	21.59	134.55	18914	6.21	1848	3067	4407	4923	13047	7389	19804	27673	24350	20366	18000	16721	16584	12960
MB-289-1 - 4	2755.2	26.70	182.50	144.85	23.16	42.41	16075	17.14	1388	2692	4224	4880	12838	7833	15833	20222	17154	12473	10069	9879	9814	7480
MB-289-1 - 5	2455.2	56.31	149.58	100.00	18.64	63.35	16151	17.68	1131	2349	3728	4234	11480	6607	15294	20637	18252	13132	10750	9960	10683	7920
MB-289-1 - 6	2155.2	32.23	160.00	98.53	19.93	34.21	15946	10.18	1473	2496	4063	4792	11980	7389	15441	20360	16829	12656	10813	10283	10248	7560
MB-289-1 - 7	2127.6	36.31	175.42	116.91	19.91	34.40	16204	4.43	1181	2305	3922	4707	12169	7371	14853	18781	15488	10989	9256	9028	8553	6172
MB-289-1 - 8	513.8	11.07	36.17	23.53	4.61	11.05	32903	2.43	608	1409	2996	3919	10845	6536	12108	14349	11260	7271	5538	5215	5770	3684
MB-289-1 - 9	136.6	4.08	17.21	4.63	4.41	7.09	33763	2.51	158	1062	2683	3667	10027	6163	11471	13740	10569	6978	5263	4907	5311	3412
MB-289-1 - 10	559.0	9.13	36.38	21.03	4.61	9.03	31290	2.38	776	1424	2920	3757	10405	6270	11961	14598	10976	7546	5556	5259	5497	3872
MB-289-1 - 11	181.4	7.38	23.54	8.90	4.07	7.43	32473	2.35	208	1170	2813	3726	10209	6270	11701	13657	10935	7106	5494	5190	5435	3532
MB-289-1 - 12	142.1	6.12	19.54	3.68	4.82	8.69	33333	2.64	199	1153	2802	3845	10243	6252	11569	13767	11220	7070	5450	5089	5540	3552
MB-289-1 - 13	782.8	14.85	42.67	34.56	5.27	19.90	32473	3.48	511	1525	2985	3915	10345	6519	11961	13961	10854	7198	5569	5304	5466	3496
MB-289-1 - 14	227.9	6.80	23.04	7.79	4.36	10.60	30344	2.43	367	1228	2823	3869	10966	6501	12113	14820	11667	7271	5550	5263	5435	3636
MB-289-1 - 15	179.3	6.50	7.46	2.43	3.55	9.69	36344	3.17	171	1101	2866	3578	10176	6359	11618	14017	10528	7106	5400	4903	5522	3532
MB-289-1 - 16	279.7	10.49	17.67	9.34	4.04	13.56	32473	2.46	667	1480	2877	3786	10385	6377	12304	14488	11179	7308	5906	5563	5907	3924
MB-289-1 - 17	86.9	7.18	7.96	2.94	3.13	9.58	35054	3.23	443	1243	2694	3746	10223	6341	11765	14100	10850	7125	5506	5235	5789	3652
MB-289-1 - 18	102.4	8.35	6.17	0.76	2.86	9.95	39355	3.06	257	1101	2586	3573	9845	6306	11373	13518	10610	7216	5369	5065	5739	3620
MB-289-1 - 19	236.2	13.20	5.25	2.28	2.93	18.22	35699	6.21	679	1432	2802	3753	9973	6519	11765	14238	10935	7491	5756	5559	5944	3720
MB-289-1 - 20	195.9	12.62	4.58	1.84	2.52	16.68	39892	2.58	191	1104	2640	3641	10169	6359	11652	14820	11220	7527	5788	5356	5795	3812
MB-289-1 - 21	475.9	17.77	4.63	4.41	2.84	28.27	37419	2.94	418	1201	2608	3696	10014	6092	11505	13823	10894	7253	5494	5385	5652	3748

Phase diagrams showing stability field described in Fig. 2, Markl et al 2016.